

Article

Global Sensitivity Analysis of Economic Model Predictive Longitudinal Motion Control of a Battery Electric Vehicle

Matthias Braband ^{1,*}, Matthias Scherer ¹ and Holger Voos ²

¹ Department of Electrical Engineering, University of Applied Sciences Trier, Schneidershof, 54293 Trier, Germany; m.scherer@hochschule-trier.de

² Interdisciplinary Centre for Security, Reliability and Trust, University of Luxembourg, 29 Av. J.F. Kennedy, 1855 Luxembourg, Luxembourg; holger.voos@uni.lu

* Correspondence: m.braband@hochschule-trier.de

Abstract: Global warming forces the automotive industry to reduce real driving emissions and thus, its CO₂ footprint. Besides maximizing the individual efficiency of powertrain components, there is also energy-saving potential in the choice of driving strategy. Many research works have noted the potential of model predictive control (MPC) methods to reduce energy consumption. However, this results in a complex control system with many parameters that affect the energy efficiency. Thus, an important question remains: how do these partially uncertain (system or controller) parameters influence the energy efficiency? In this article, a global variance-based sensitivity analysis method is used to answer this question. Therefore, a detailed powertrain model controlled by a longitudinal nonlinear MPC (NMPC) is developed and parameterized. Afterwards, a qualitative Morris screening is performed on this model, in order to reduce the parameter set. Subsequently, the remaining parameters are quantified using Generalized Sobol Indices, in order to take the time dependence of physical processes into account. This analysis reveals that the variations in vehicle mass, battery temperature, rolling resistance and auxiliary consumers have the greatest influence on the energy consumption. In contrast, the parameters of the NMPC only account for a maximum of 5% of the output variance.

Keywords: economic MPC; BEV; generalized Sobol indices; Morris screening; variance-based sensitivity indices; electric drive system; electric vehicle



Citation: Braband, M.; Scherer, M.; Voos, H. Global Sensitivity Analysis of Economic Model Predictive Longitudinal Motion Control of a Battery Electric Vehicle. *Electronics* **2022**, *11*, 1574. <https://doi.org/10.3390/electronics11101574>

Academic Editor: Rui Castro

Received: 13 April 2022

Accepted: 11 May 2022

Published: 14 May 2022

Publisher's Note: MDPI stays neutral with regard to jurisdictional claims in published maps and institutional affiliations.



Copyright: © 2022 by the authors. Licensee MDPI, Basel, Switzerland. This article is an open access article distributed under the terms and conditions of the Creative Commons Attribution (CC BY) license (<https://creativecommons.org/licenses/by/4.0/>).

1. Introduction

Considering global warming and the targeted reduction of greenhouse gas emissions by governments, the transformation to electromobility plays an important role in reaching climate goals. Great potential to reduce these emissions lies in replacing conventional vehicle propulsion systems with electric propulsion systems, as outlined in [1]. It is shown that the change to electric vehicles avoid local emissions, which improves the air quality, especially in larger cities. Furthermore, the dependence on oil imports is reduced. Nevertheless, there are many other aspects that can reduce the energy consumption of vehicles, including environmental conditions, such as the weather or road surface conditions, the driving style of the driver and the vehicle itself [2]. Especially for battery electric vehicles (BEVs) with long recharge times and lower ranges than internal combustion engines saving energy during operation plays a crucial role. Thus, the development of energy-efficient driving strategies to reduce fuel consumption have gained significant industrial interest [3]. As a vehicle can only be optimized during the development process and usually not influenced during operations, the development of eco-driving strategies to optimize the operation of vehicles has received great attention. Eco-driving generally describes the reduction of fuel consumption by operating the vehicle along its energy-optimal velocity trajectory. It can be processed by a human driver using learned patterns to achieve low energy consumption;

for example, through smooth acceleration or deceleration and maintaining a constant speed. Furthermore, eco-driving is capable of reducing traffic fatalities and can reduce the risk of traffic accidents [3]. However, without exact knowledge of the energy-optimal operating points of the vehicle and the upcoming driving situation, a human driver can only reach a sub-optimal driving strategy.

The increasing availability of environmental data and the processing power of modern vehicle platforms has enabled the development of advanced eco-driving algorithms, which consider environmental information and the actual vehicle state to optimize the driving strategy. To address this multi-objective target, most approaches focus on model predictive controllers (MPC) as a promising optimization approach for real-time optimal control. MPCs are often designed as a linear quadratic problem to achieve real-time capability [4–7]. This simpler—but computationally effective—design usually leads to simplifications of the system model of the MPC. In [4,5], the energy consumption of the underlying powertrain components was approximated using a convex lookup table. Combined spatial–temporal modeling to ensure a linear optimization problem has been proposed in [7]. Furthermore, explicit solutions for the driving strategy (see, e.g., [6]) involve solving the optimization problem offline and storing the results in a lookup table.

To overcome these approximations, nonlinear MPC (NMPC) approaches [8–14] have been outlined in the literature. These approaches ensure more accurate modeling of the control problem. To ensure real-time capability, the nonlinear approaches are often solved using dynamic programming [10,11] or calculated online using an efficient NMPC solver [8,9,12,14], such as C/GMRES. Furthermore, stochastic approaches, mainly for modeling the non-deterministic surrounding traffic, have also been presented in the literature [15–19].

The application of MPC based longitudinal motion control has been applied to internal combustion engine vehicles [6,8,9], hybrid electric vehicles [13,14], and pure electric vehicles [4,5,7,10,12,15–17].

All of the approaches mentioned above are complex closed-loop control systems with a large number of system and controller parameters, which all influence the system behavior. Therefore, the important question remains: how can the influence of parameters on the energy consumption and the driving behavior be quantified, which normally cannot be done analytically in such complex systems? To answer this question, qualitative- and quantitative-based sensitivity analysis methods to analyze and quantify parameter dependencies have been proposed in the literature. The most popular and promising methods are qualitative Morris parameter screening [20] and the variance-based sensitivity analysis, first introduced by Sobol [21]. In particular, in the context of analyzing the energy efficiency of BEVs several studies exist which highlight the potential of statistical investigation. In the work of [22], parameter dependencies on the energy efficiency were investigated during a field test with six buses on three different routes using regression coefficients. Furthermore, [23] have outlined a surrogate model to predict the energy consumption of electrical buses and performed a sensitivity analysis to determine parameter dependencies in their prediction using Sobol indices. A sensitivity analysis of a BEV using Sobol indices has been outlined in [24], which was performed on previously recorded velocity profiles for typical urban and rural use-cases in the Vienna area. Nevertheless, this work is based on a simple longitudinal motion model only considering efficiency rates in the electric drivetrain. More detailed sensitivity analyses on specific drivetrain components and not at the vehicle level have been conducted in [25–28]. In [25], a qualitative Morris screening was performed to analyze a basic equivalent circuit model of a battery system. A Morris screening-based investigation considering the reaction kinematic models of a battery has been detailed in [26]. Parameter dependencies on the torque accuracy of an electric drive system using Sobol indices have been outlined in [27]. Furthermore, a good review regarding sensitivity analysis for electrical drives can be found in [28]. Beside the aforementioned applications [29] have underlined the increasing demand for systematic analyses of complex mathematical models across different disciplines.

However, the aforementioned publications at vehicle level have not included detailed powertrain models, whereas the component-level evaluations did not take dependencies at the system level into account. Furthermore, the outlined investigations were carried out using pre-recorded velocity profiles at vehicle level or specific working points or load profiles at component level. Therefore, this article outlines a novel approach for analyzing a closed-loop economic NMPC-based eco-driving system of a BEV using Morris screening and variance-based sensitivity analysis. Furthermore, in contrast to the known literature, the drivetrain components considered in this investigation are modeled in great detail, and are optimized with respect to accuracy and calculation time, in order to obtain reliable sensitivity results. Furthermore, the time dependence of physical processes is considered in the sensitivity analysis, through the use of Generalized Sobol indices [30].

The remainder of this article is organized as follows: Section 2 outlines the theory of the used sensitivity analysis methods of Morris Screening, Sobol indices and Generalized Sobol Indices. In Section 3, the developed and used simulation models are presented. Section 4 presents the economic NMPC used in this investigation. In Section 5, the sensitivity analysis setup is defined and in Section 6, the results of the sensitivity analysis are discussed. Section 7 concludes the presented findings of this article.

2. Sensitivity Analysis

The process of a variance-based sensitivity analysis is shown in Figure 1. Based on the uncertainties of different model parameters $\mathbf{X} = [X_1, X_2, \dots, X_k]$, described by their probability density functions, a classical uncertainty analysis is performed. This is usually done by carrying out a Monte-Carlo simulation, where the result is a distribution of the model output Y . However, in an uncertainty analysis, no conclusions can be drawn about the cause of the variance. The sensitivity analysis closes this gap and enables a quantification of the influencing factors. This makes it possible to specifically influence the relevant parameters, thus reducing the output variance. As the quantitative variance-based sensitivity analysis (outlined in Section 2.2) is a computationally expensive task, qualitative Morris screening [20] is used in advance, in order to identify parameters that have nearly no effect on the output of interest. Therefore, the computational burden of the quantitative analysis is reduced by neglecting non-influential parameters from the simulation study.

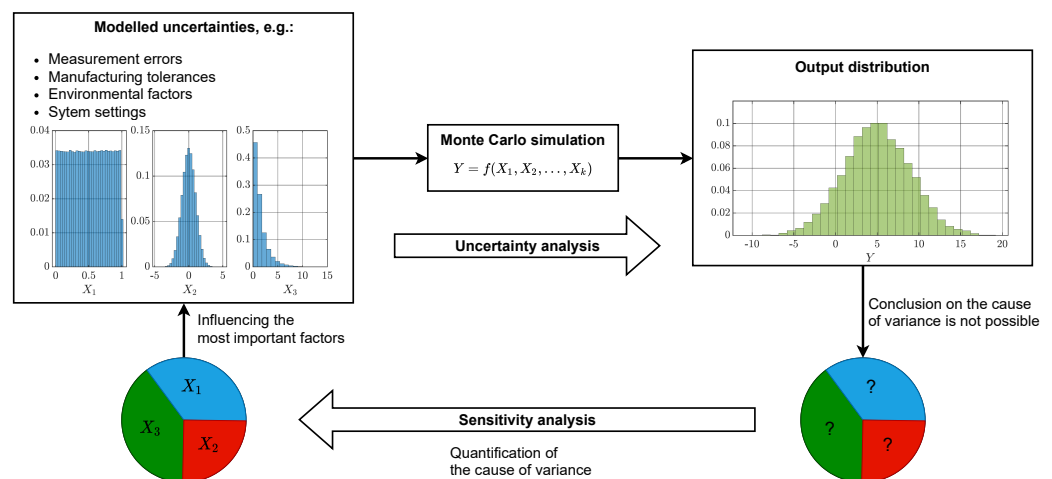


Figure 1. Process of a variance-based sensitivity analysis. The difference between an uncertainty analysis and a sensitivity analysis is also outlined.

2.1. Morris Screening

Morris Screening, according to [20], offers an efficient method for the qualitative estimation of the influences of parameters on a model output. The main idea is based on the elementary effect

$$EE_i = \frac{f(x_1, x_2, \dots, x_{i-1}, x_i + \Delta, x_{i+1}, \dots, x_k) - f(\mathbf{x})}{\Delta} \tag{1}$$

for a given model $y = f(\mathbf{x})$, with y as the model output and $\mathbf{x} = [x_1, x_2, \dots, x_k]$ as the parameter input vector. Due to the addition of the small variation Δ to the i th parameter and in the denominator, the elementary effect can be understood as a partial difference quotient. This OAT-design needs to be calculated $k + 1$ times to obtain one elementary effect for each parameter. In [20], a novel scheme for defining the trajectory through this input parameter space was proposed. However, using only one elementary effect calculation for each parameter does not provide a satisfactory covering of the input parameter space. Therefore, the calculation of elementary effects is done for r different input trajectories with varying starting points. This results in $N_m = r(k + 1)$ needed simulation runs, where [31,32] have shown that $r = 10$ is a typical value for producing valuable results.

As sensitivity measures, the mean μ_i , the mean of the absolute values μ_i^* and the standard deviation σ_i of the elementary effects are considered. The measures

$$\mu_i = \frac{1}{r} \sum_{j=1}^r EE_i^j \tag{2}$$

and

$$\sigma_i = \sqrt{\frac{1}{r-1} \sum_{j=1}^r (EE_i^j - \mu_i)^2} \tag{3}$$

were first presented in [20]. Here, μ_i assesses the overall influence of the i th parameter on the output, whereas σ_i is an effective measure to estimate nonlinear or interaction effects in the model. However, using the proposed measure μ_i has the disadvantage that type II errors can occur, which may result in failing to identify factors with considerable influence on the output. The measure

$$\mu_i^* = \frac{1}{r} \sum_{j=1}^r |EE_i^j|, \tag{4}$$

first introduced by [33], avoids type II errors by using the absolute values of the elementary effects.

The measures presented above are used to rank the importance of the parameters. Small values of μ_i^* in relation to other parameters indicate a small influence on the output and so, such parameters can be neglected in the quantitative sensitivity setup. In contrast, large values in comparison to the other parameters express a strong influence and the related parameters must be considered in the quantitative sensitivity setup.

2.2. Variance-Based Sensitivity Analysis

As outlined in [21], the idea of a variance-based sensitivity analysis is the decomposition of a model $y = f(\mathbf{x})$ with $\mathbf{x} = [x_1, x_2, \dots, x_k]$ in a sum of 2^k terms using a High-Dimensional Model Representation (HDMR) in the form

$$y = f(\mathbf{x}) = f_0 + \sum_{i=1}^k f_i(x_i) + \sum_{i=1}^k \sum_{i < j}^k f_{ij}(x_i, x_j) + \dots + f_{12\dots k}(x_1, x_2, \dots, x_k), \tag{5}$$

where f_0 describes a constant term without any dependencies on the input vector, whereas the k terms $f_i(x_i)$ describe first-order functions with dependencies on only one input parameter x_i . This scheme can be continued up to $\binom{n}{k} = \frac{n!}{k!(n-k)!}$ terms, representing n th

order functions with dependencies on n input parameters. Assuming independence of the parameters and orthogonality of the terms in (5), the variance is given by

$$\begin{aligned}
 V(Y) &= \int_{-\infty}^{\infty} \cdots \int_{-\infty}^{\infty} (f(\mathbf{x}) - f_0)^2 \prod_{m=1}^k p_m(X_m) d\mathbf{x} \\
 &= \sum_{i=1}^k V_i + \sum_{i=1}^k \sum_{i < j}^k V_{ij} + \dots + V_{12\dots k},
 \end{aligned}
 \tag{6}$$

with p_m being the probability density function of the corresponding input parameter X_m . The variances of the corresponding terms are defined by

$$V_i = V(f_i(x_i)) = \int_{-\infty}^{\infty} f_i^2(x_i) p_i(X_i) dx_i
 \tag{7}$$

$$V_{ij} = V(f_{ij}(x_i, x_j)) = \int_{-\infty}^{\infty} \int_{-\infty}^{\infty} f_{ij}^2(x_i, x_j) p_i(X_i) p_j(X_j) dx_i dx_j
 \tag{8}$$

⋮

$$V_{12\dots k} = V(f_{12\dots k}(x_1, x_2, \dots, x_k)) = \int_{-\infty}^{\infty} \cdots \int_{-\infty}^{\infty} f_{12\dots k}^2(x_1, x_2, \dots, x_k) \prod_{m=1}^k p_m(X_m) d\mathbf{x}.
 \tag{9}$$

Normalizing (6) by $V(Y)$ leads to

$$1 = \sum_{i=1}^k S_i + \sum_{i=1}^k \sum_{i < j}^k S_{ij} + \dots + S_{12\dots k},
 \tag{10}$$

which serves as a decomposition of the source of variance. The terms containing S_i are referred to as first-order effects. They quantify the influence of the parameter x_i without interactions to other parameters to the output y . S_{ij} denotes the second-order effects, which indicate the interaction between two parameters x_i, x_j . This decomposition scheme can be continued up to the k th-order effects.

Another useful measure, especially for describing all nonlinear interaction effects, is the total effect

$$S_{Ti} = S_i + \sum_{\substack{j=1 \\ j \neq i}}^k S_{ij} + \dots + S_{12\dots k},
 \tag{11}$$

which sums up all effects of one parameter, including all higher-order effects.

As outlined in [34], the first-order indices can be calculated using the relation of the conditional expectation value $V_{X_i}(E_{\mathbf{X}_{\sim i}}(Y | X_i))$ and the overall variance $V(Y)$, described by

$$S_i = \frac{V_{X_i}(E_{\mathbf{X}_{\sim i}}(Y | X_i))}{V(Y)},
 \tag{12}$$

where $\mathbf{X}_{\sim i}$ denotes the vector of all parameters except X_i . The expectation operator $E_{\mathbf{X}_{\sim i}}(\cdot)$ calculates the average over $\mathbf{X}_{\sim i}$, whereas X_i is fixed and the outer variance $V_{X_i}(\cdot)$ is taken over all realizations of X_i .

The total effect is calculated using [34,35]

$$S_{Ti} = \frac{E_{\mathbf{X}_{\sim i}}(V_{X_i}(Y | \mathbf{X}_{\sim i}))}{V(Y)} = 1 - \frac{V_{\mathbf{X}_{\sim i}}(E_{X_i}(Y | \mathbf{X}_{\sim i}))}{V(Y)}.
 \tag{13}$$

An obvious explanation is to consider that $V_{\mathbf{X}_{\sim i}}(E_{X_i}(Y | \mathbf{X}_{\sim i}))$ is the first-order effect of $\mathbf{X}_{\sim i}$. Consequently, $V(Y) - V_{\mathbf{X}_{\sim i}}(E_{X_i}(Y | \mathbf{X}_{\sim i}))$ must include all terms in the variance decomposition of (6) which include X_i .

The decomposition presented in (5) leads to $2^k - 1$ possible sensitivity measures. Due to the large number of indices, it is impractical to analyze all of them. Nevertheless, the first-order and the total effects approximate the system behavior satisfactorily, such that higher-order effects can usually be neglected. In addition, estimation of the conditional expectation values using Monte-Carlo simulations is computationally expensive and therefore, only the first-order and total effects are considered.

The indices can be interpreted as the expected reduction of variance. The numerator of the first order effects $V_{X_i}(E_{\mathbf{X}_{\sim i}}(Y | X_i))$ describes the reduction of variance in the output Y if X_i were fixed at some defined value. Furthermore, the numerator of the total effect $E_{\mathbf{X}_{\sim i}}(V_{X_i}(Y | \mathbf{X}_{\sim i}))$ is the amount of variance that would remain if all factors but X_i were fixed. The ordering of the sensitivity measures quantify their contribution to the overall variance. In other words, small sensitivity measures have only a small influence on the variance of the output, whereas large measures have a big influence on the output. Moreover, the sensitivity measures have some general properties which are useful to analyze the structure of the model:

- Due to (10), the condition $\sum_{i=1}^k S_i \leq 1$ holds.
- Due to (11), the condition $\sum_{i=1}^k S_{T_i} \geq 1$ holds.
- If $\sum_{i=1}^k S_i = 1$, the model is additive.
- If $1 - \sum_{i=1}^k S_i \gg 0$, the model has nonlinear behavior or interacting parameters.
- If $S_{T_i} \approx S_i$, no interactions exists. This also implies the additivity of the model.
- If $S_{T_i} \approx 0$, the parameter has no influence on the output.

2.3. Time and State Dependency of Technical Processes

The main drawback of the HDMR described in (5) is that it neglects state and time dependencies, regarding the physical systems. Thus, the underlying model needs to be expanded to

$$y(t) = f(\mathbf{x}, \mathbf{x}_0, t, \mathbf{u}(t)), \tag{14}$$

where \mathbf{x}_0 denotes the initial system state. Furthermore, the system consists of a control vector $\mathbf{u} = [u_1, u_2, \dots, u_c]$, with c being the number of control inputs. The proposed extension by \mathbf{x}_0, t and $\mathbf{u}(t)$ leads also to state- and time-dependent sensitivity indices. As already outlined in [27], the dependency of \mathbf{x}_0 and $\mathbf{u}(t)$ can be ensured by covering all the relevant operating points of the physical system. In this article, this is ensured by defining representative drive cycles, as outlined in Section 3.4. Thus, (14) can be simplified to

$$y(t) = f(\mathbf{x}, t) \tag{15}$$

and can also be written as a second-order ANOVA-like decomposition

$$f(\mathbf{x}, t) = f_U(\mathbf{x}_U, t) + f_{U^c}(\mathbf{x}_{U^c}, t) + f_{U, U^c}(\mathbf{x}, t), \tag{16}$$

with the complete index set $X = \{1, \dots, k\}$, the subset $U = \{i_1, i_2, \dots, i_s\} \subset X$ and the complementary subset $U^c = \{j_1, j_2, \dots, j_s\} = X \setminus U$. The corresponding parameter vectors are $\mathbf{x}_U = [x_{i_1}, x_{i_2}, \dots, x_{i_s}]$ and $\mathbf{x}_{U^c} = [x_{j_1}, x_{j_2}, \dots, x_{j_s}]$. The variance of this decomposition is defined as

$$V(f, t) = V_U(f, t) + V_{U^c}(f, t) + V_{U, U^c}(f, t), \tag{17}$$

where $V_U = V_i$ holds if the subset U contains only the i th parameter. In this case (17) is equal to (6). In the following, the subset containing only the i th parameter is denoted by U_i .

The Sobol indices are usually calculated as point-in-time indices. For the scalar case with $V_{U_i} = V_i$, the sensitivity indices can be expressed as follows

$$S_i(f, t) = \frac{V_{U_i}(f, t)}{V(f, t)} \tag{18}$$

$$S_{T_i}(f, t) = \frac{V_{U_i}(f, t) + V_{U_i, U_{\sim}}(f, t)}{V(f, t)} \quad (19)$$

for each $t \in [0, T]$. There are several problems when using only these point-in-time estimates [30]:

- Point-in-time indices ignore all time correlations of the process.
- The variance of the process varies in time, which skews the relative importance across time.

To solve the above-mentioned issues, [30] introduced the Generalized Sobol Indices, which are based on a covariance operator to take the evolution of the process over time into account. Furthermore, the second issue regarding skewing is solved by this approach. The Generalized Indices are defined as

$$S_i^G(f, T) = \frac{\int_0^T V_{U_i}(f, t) dt}{\int_0^T V(f, t) dt} \quad (20)$$

$$S_{T_i}^G(f, T) = \frac{\int_0^T (V_{U_i}(f, t) + V_{U_i, U_{\sim}}(f, t)) dt}{\int_0^T V(f, t) dt}, \quad (21)$$

which can be simply computed using the approximation

$$S_i^G(f, T) \approx \frac{\sum_{m=1}^N w_m V_{U_i}(f, t_m)}{\sum_{m=1}^N w_m V(f, t_m)} \quad (22)$$

$$S_{T_i}^G(f, T) \approx \frac{\sum_{m=1}^N w_m (V_{U_i}(f, t_m) + V_{U_i, U_{\sim}}(f, t_m))}{\sum_{m=1}^N w_m V(f, t_m)} \quad (23)$$

in a numerical setup with weights $\{w_m\}_{m=1}^N$ for each node $\{t_m\}_{m=1}^N$. The special case of equal weights and uniform time steps has been suggested in [36] for time-dependent processes, which is used throughout this article. The indices are calculated using the estimators described in [34] and convergence of this estimators is ensured as proposed in [27].

3. Simulation Setup

The vehicle serving as the basis for this simulation study is an early-stage prototype for urban and inter-urban use-cases, which is under development at the University of Applied Sciences Trier. A sketch of the proTRon Evolution is provided in Figure 2. The project focuses on sustainable mobility, taking into consideration the complete product life cycle. Due to this fact, the vehicle body is largely made of natural fiber-reinforced plastics, in order to reduce emissions in the manufacturing process. In order to keep energy consumption in driving operations as low as possible, a target weight of 550 kg is planned while, at the same time, complying with the crash safety requirements relevant for approval. Furthermore, all mechanical driving resistances are forced to be as small as possible. This is achieved by using tires with low rolling resistance properties with dimensions 115/80 R 15, in order to reduce the rolling resistance coefficient. Additionally, the aerodynamic drag coefficient and the frontal area of the vehicle were minimized during the development process using CFD simulations, resulting in low aerodynamic resistance. Furthermore, the car uses a novel transmission concept, consisting of a belt drive and a planetary gear with optimized losses within a small installation space. The powertrain of the vehicle consists of a single-wheel drive on the rear axle with EMRAX 188 permanent magnet synchronous drives, which are powered by a series connection of 76 40 Ah Winston WB-LYP40AHA lithium iron phosphate accumulators.



Figure 2. Sketch of the proTRon Evolution.

The used simulation setup, including the configuration of the BEV, is outlined in Figure 3. As the underlying component models can highly affect the sensitivity analysis results, they are a crucial part of the simulation setup. Therefore, the models commonly used in the literature are modified with the aim of increasing accuracy and minimizing computation time. In particular, the inverter and electric drive models are optimized, regarding calculation time, to fit into the Monte-Carlo setup of the sensitivity analysis by averaging the losses over one fundamental wave period and neglecting the current dynamics in the electrical drive model. Furthermore, the inverter model is extended to precisely model nonlinear switching losses, especially for low currents. To improve the accuracy of the electrical drive model nonlinear iron losses are taken into account. For the aforementioned reasons and in order to emphasize the nonlinear parameter dependencies of the battery, the battery, inverter and electrical drive component models', as well as their corresponding parameters are discussed in detail in the following. As the vehicle model is a standard longitudinal motion model, the details are only outlined in Appendix A. The environmental model consists of a route model, including curvature, slope and legal speed limit information. Furthermore, the ambient temperature and air pressure are provided to the simulation environment.

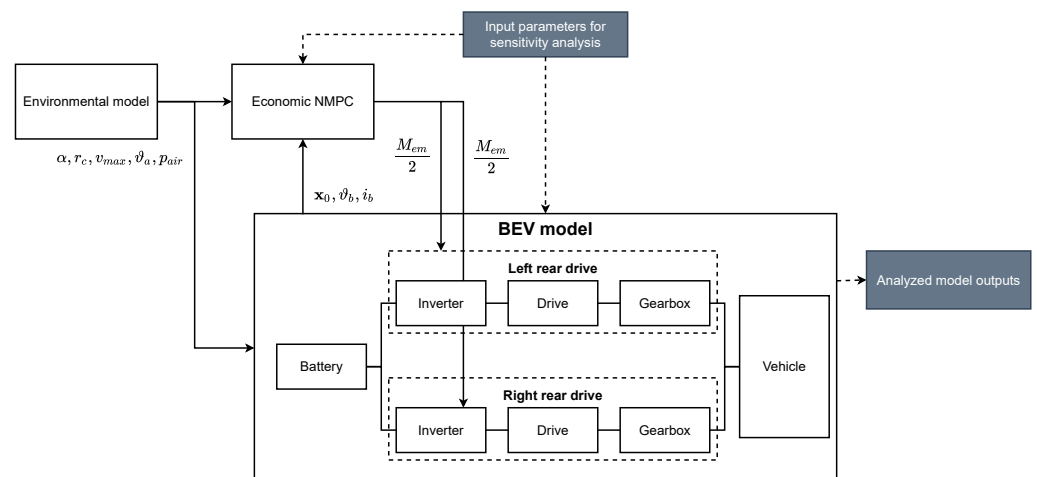


Figure 3. Simulation setup of the proposed BEV.

3.1. Battery Model

Modeling the behavior of a modern lithium ion accumulator can be divided according to different complexities and different levels of model knowledge. White-box models based on reaction kinetics [37,38] or physically motivated equivalent circuit modeling [39] provide a detailed basis for understanding the electrochemical processes. However, the complexity of such models also significantly increases the computational cost and parameterization is often only possible with high effort. In contrast, black-box models, such

as neural networks [40] and Markov chains [41], may also be used. They are easy to train or parameterize from existing measurement data. However, the major drawback of these modeling is a lack of representation of physical relationships. In order to reduce the complexity without losing a general physical interpretability of the models, simple equivalent circuit models have been established. These range from a simple representation with constant voltage source and internal resistance [42] to electrical RC networks with operating point-dependent parameters [43]. Due to the possible physical interpretability of the parameters, good parameterizability and low computation times, a corresponding equivalent circuit model is used and introduced in the following.

3.1.1. Electrical Model

Figure 4 depicts the equivalent circuit diagram of a single battery cell. It consists of a voltage source u_{OCV} , a series resistor R_s representing the ohmic losses in the battery cell, and two RC elements describing the cell dynamics. The terminal voltage is calculated using Kirchhoff’s mesh rule, with

$$u_k = n_{cell}(u_{OCV} - u_{R_s} - u_{RC1} - u_{RC2}), \tag{24}$$

where n_{cell} denotes the number of cells connected in series. Using Kirchhoff’s junction rule, the differential equations for the required voltage drops u_{RC1} and u_{RC2}

$$\dot{u}_{RC1} = \frac{i_b - \frac{u_{RC1}}{R_1(SoC, I_b, \vartheta_b)}}{C_1(SoC, I_b, \vartheta_b)} \tag{25}$$

$$\dot{u}_{RC2} = \frac{i_b - \frac{u_{RC2}}{R_2(SoC, I_b, \vartheta_b)}}{C_2(SoC, I_b, \vartheta_b)} \tag{26}$$

can be obtained. Furthermore, the voltage drop on the series resistance is defined by

$$u_{R_s} = R_s(SoC, i_b, \vartheta_b)i_b. \tag{27}$$

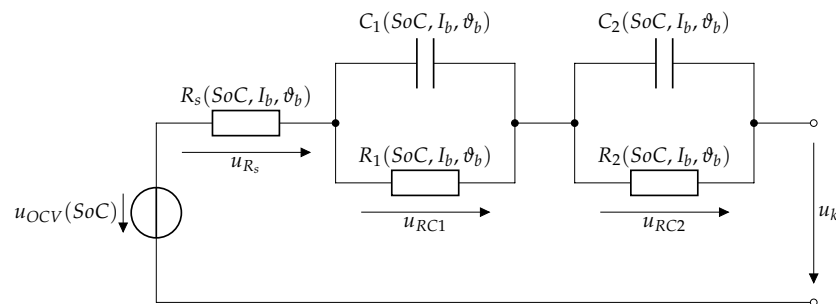


Figure 4. Electrical equivalent circuit model of the battery.

As it can be seen from (25)–(27), as well as from the outlined parameter maps in Figure 5, the parameters R_s, R_1, R_2, C_1 and C_2 depend on the actual operating point of the battery cell, which is defined by the State of Charge (SoC)

$$SoC = \frac{Q_{SoC}}{Q_b(\vartheta_b)}, \tag{28}$$

the battery current i_b and the battery temperature ϑ_b . Q_{SoC} defines the actual stored electrical charge, whereas Q_b is the maximum available electrical charge of one cell. Furthermore, the open circuit voltage u_{OCV} depends on the actual SoC and Q_b is influenced by ϑ_b , as outlined in Figure 6. The aforementioned electrical parameters of the used battery cells were acquired from [44] and are outlined in Figures 5 and 6.

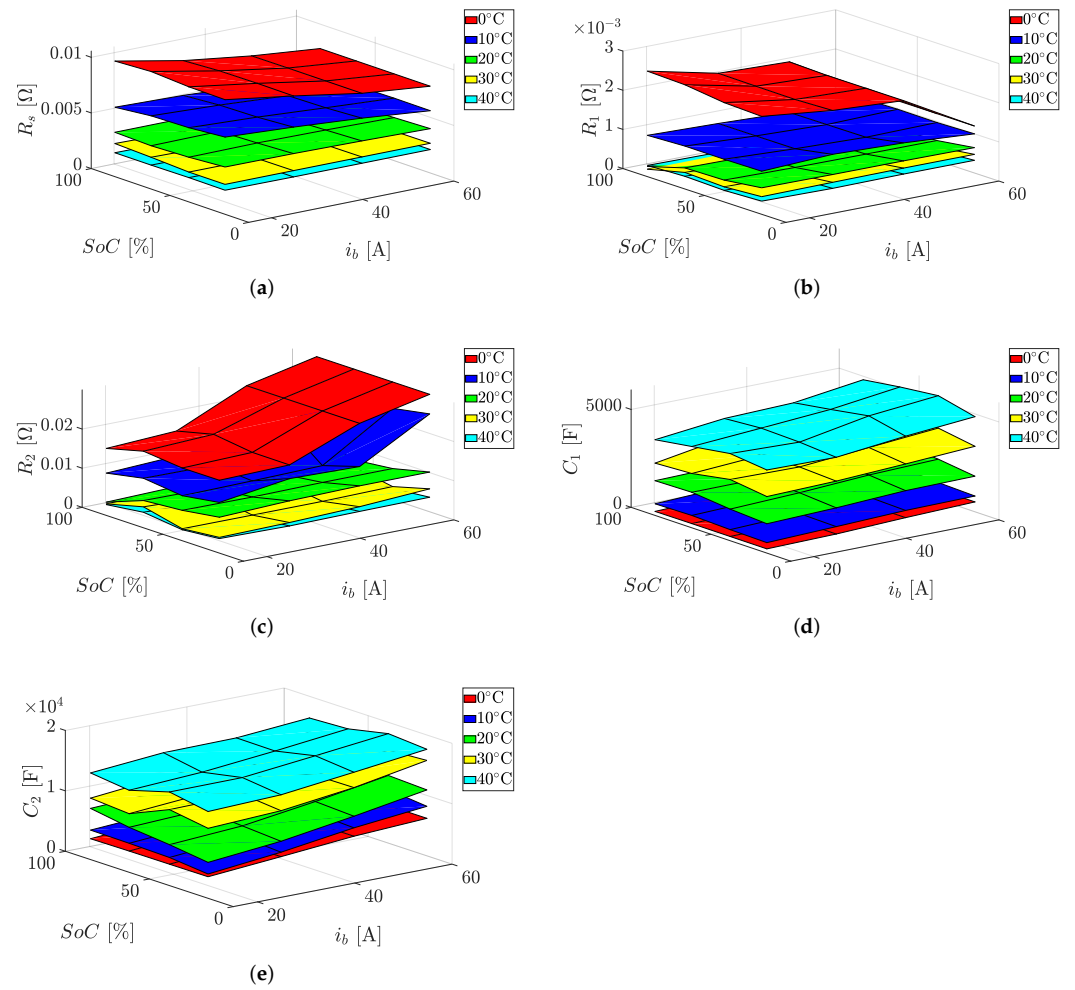


Figure 5. Electrical battery parameters, according to [44]. (a) R_s ; (b) R_1 ; (c) R_2 ; (d) C_1 ; (e) C_2 .

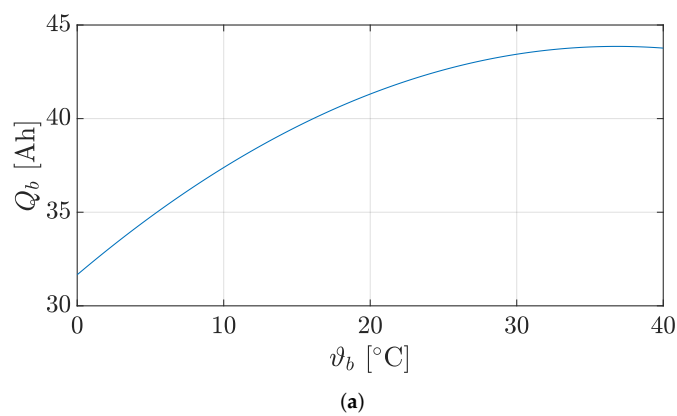


Figure 6. Cont.

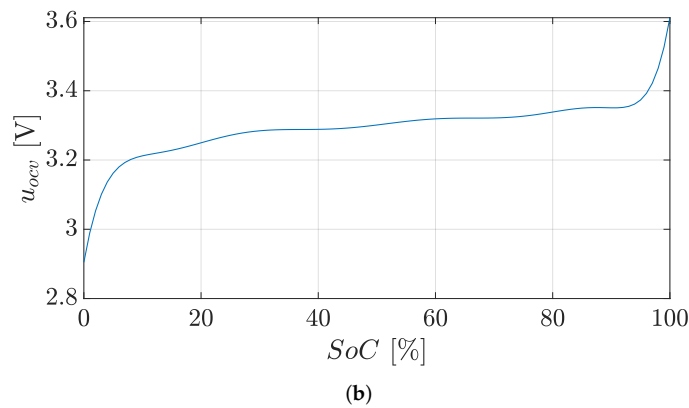


Figure 6. Battery capacity and open circuit voltage, according to [44]. (a) Battery capacity; (b) Open circuit voltage.

3.1.2. Thermal Model

Figure 7 outlines the model used for the thermal behavior of a battery cell. In Figure 7a, the cross-section of one cell is outlined. The red part in this scheme consists of the battery housing and the reactive part of the cell, including the anode, cathode, separator and electrolyte, whereas the yellow part describes the metallic connection of the cell core to the terminals. The corresponding heat capacities are assigned to the two areas of the cell. C_c describes the heat capacity of the cell core, while the heat capacities of the two terminals are combined into one heat capacity C_t . The dominant heat transfers to the surrounding air take place between the battery core and ambient air through R_{thca} and between the terminals and ambient air through R_{thta} . Likewise, R_{thct} represents the remaining heat transfer between the cell core and the terminals. Given the battery loss $P_{v,b}$ caused by the ohmic losses on R_s , R_1 and R_2 the thermal behavior can be described by

$$\dot{\vartheta}_b = \frac{P_{v,b} - \frac{\vartheta_b - \vartheta_{air}}{R_{thca}} - \frac{\vartheta_b - \vartheta_t}{R_{thct}}}{C_c} \quad (29)$$

and

$$\dot{\vartheta}_t = \frac{\frac{\vartheta_b - \vartheta_t}{R_{thct}} - \frac{\vartheta_t - \vartheta_{air}}{R_{thta}}}{C_t}, \quad (30)$$

using Kirchhoff's junction rule. The thermal capacities C_c and C_t are determined using the percentage composition of the core and terminal materials, with respect to their associated specific heat capacities. The heat transfer resistances R_{thca} , R_{thct} and R_{thta} are composed of the heat transfer characteristics of each internal layer of the battery, the housing and the terminals. In addition to the internal transitions, the heat transfer to the outside air is also taken into account for R_{thca} and R_{thta} . The used thermal resistances can be found in [45].

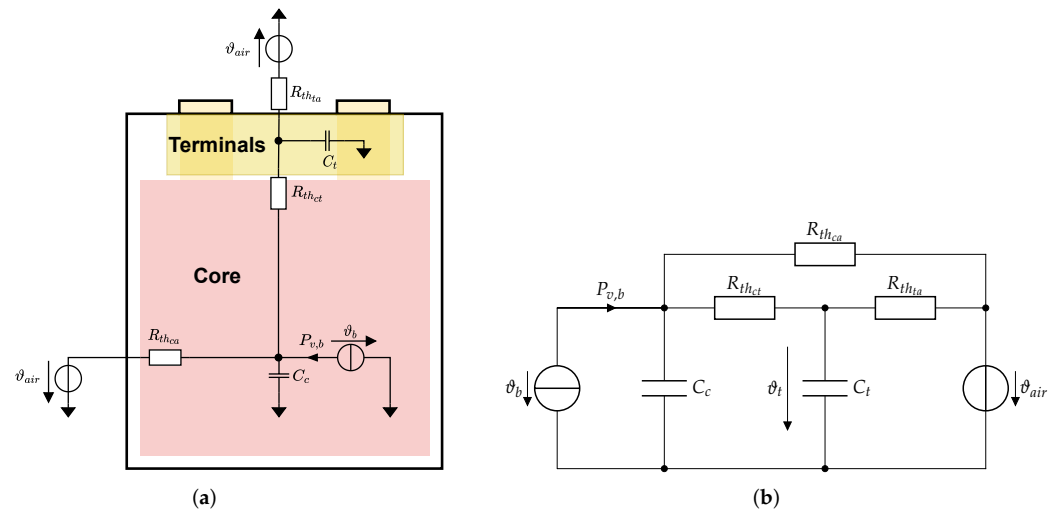


Figure 7. Thermal equivalent circuit model of the battery (a) 2D thermal model, (b) Equivalent circuit model.

3.2. Inverter Model

In the proposed system, a Voltage Source Inverter (VSI) is used. The equivalent circuit diagram of the power electronics is outlined in Figure 8. The AC side of the inverter is composed of an Insulated Gate Bipolar Transistor (IGBT) full bridge with an anti-parallel free-wheeling diode on each IGBT device. The output terminal voltages u_U, u_V and u_W , with their corresponding currents i_U, i_V and i_W , represent the interface to the electric drive. In order to generate a frequency and amplitude variable AC voltage from the DC-link voltage, the IGBTs must be switched, according to a defined pattern, using Pulse Width Modulation (PWM). Due to this switching pattern, the losses in the inverter consist of conduction and switching losses that depend on the used modulation scheme [46], which is a sine modulation with zero offset to improve the voltage utilization [47]. Due to the symmetric structure of the inverter, the loss behavior of the semiconductors differs only with a shift in time. Thus, the power dissipation models can be reduced to one IGBT and one diode, which are applied for all semiconductors afterwards.

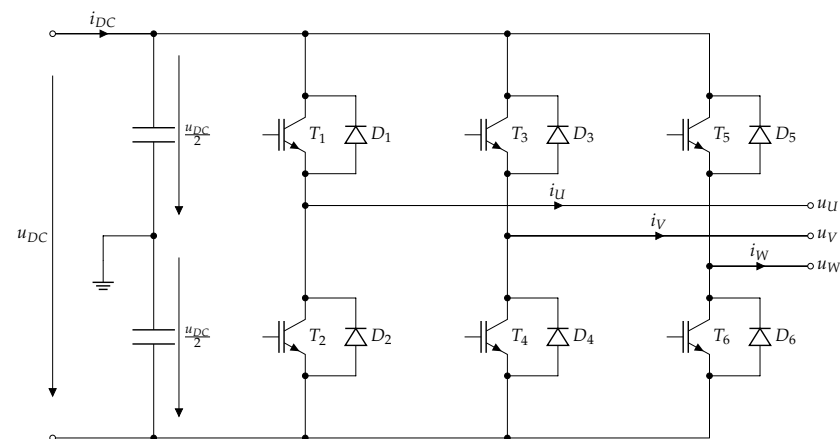


Figure 8. VSI equivalent circuit.

3.2.1. Conduction Losses

Calculation of the conduction losses is carried out for the IGBT and diode pair T_1, D_2 from Figure 8. The forward characteristics of the used power electronics are shown in

Figure 9. The power loss caused by the nonlinear resistive behavior of the semiconductors can be described using a second-order phase current-dependent polynomial [48,49]

$$\tilde{p}_{c,T_1} = a_{c,T}(\vartheta_{j,T}) \cdot i_{T_1} + b_{c,T}(\vartheta_{j,T}) \cdot i_{T_1}^2 \tag{31}$$

$$\tilde{p}_{c,D_2} = a_{c,D}(\vartheta_{j,D}) \cdot i_{D_2} + b_{c,D}(\vartheta_{j,D}) \cdot i_{D_2}^2, \tag{32}$$

with $a_{c,T}(\vartheta_{j,T})$, $b_{c,T}(\vartheta_{j,T})$ and $a_{c,D}(\vartheta_{j,D})$, $b_{c,D}(\vartheta_{j,D})$ as IGBT and diode junction temperature-dependent fitting coefficients.

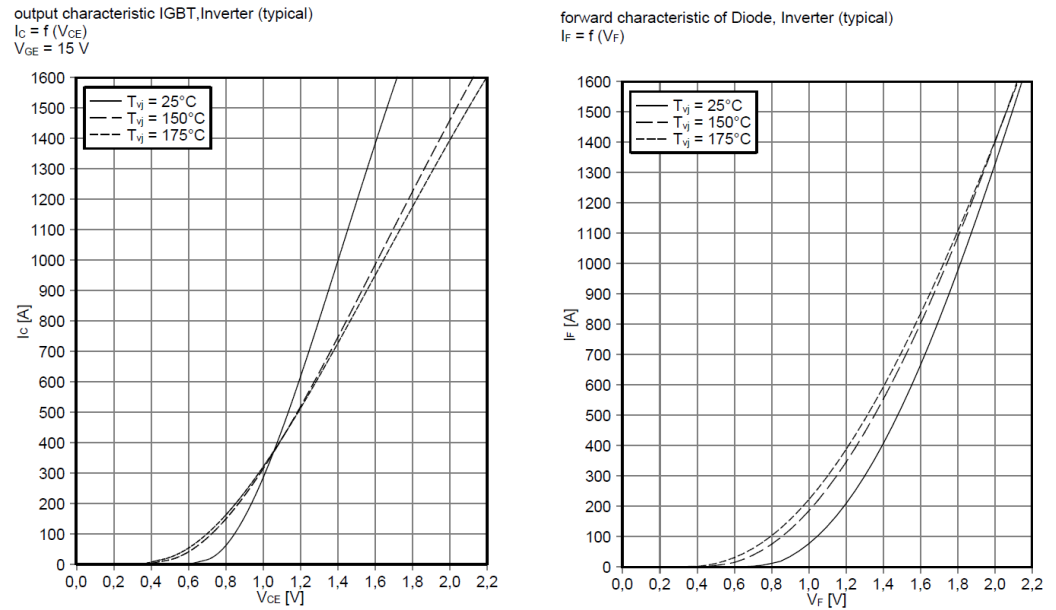


Figure 9. Forward characteristics of the used IGBT module [50].

The conduction power losses also depend on the modulation method or, respectively, on the relative conduction periods of each IGBT and diode during one commutation interval [46]. The used sine modulation with zero offset can be approximated by adding third-order harmonics to the standard sine modulation, which leads to the relative turn on times

$$\beta_{T_1} = \frac{1}{2} + \frac{M_1}{2} \cos(\varphi_{el}) + \frac{M_3}{2} \cos(3\varphi_{el}) \tag{33}$$

$$\beta_{D_2} = \frac{1}{2} - \frac{M_1}{2} \cos(\varphi_{el}) - \frac{M_3}{2} \cos(3\varphi_{el}), \tag{34}$$

where M_1 and M_3 are the corresponding modulation indices and φ_{el} describes the phase angle between the current and voltage in one inverter leg. Assuming the currents to be sinusoidal without higher-order harmonics, the conduction losses for the used modulation scheme can be described by

$$P_{c,T_1} = \frac{a_{c,T}(\vartheta_{j,T}) \hat{I}_N}{2} \left(\frac{1}{\pi} + \frac{M_1}{4} \cos(\varphi_{el}) \right) + b_{c,T}(\vartheta_{j,T}) \hat{I}_N^2 \left(\frac{1}{8} + \frac{M_1}{3\pi} \cos(\varphi_{el}) + \frac{M_3}{15\pi} \cos(3\varphi_{el}) \right) \tag{35}$$

for the IGBT and in a similar manner for the diode with

$$P_{c,D_2} = \frac{a_{c,D}(\vartheta_{j,D}) \hat{I}_N}{2} \left(\frac{1}{\pi} - \frac{M_1}{4} \cos(\varphi_{el}) \right) + b_{c,D}(\vartheta_{j,D}) \hat{I}_N^2 \left(\frac{1}{8} - \frac{M_1}{3\pi} \cos(\varphi_{el}) - \frac{M_3}{15\pi} \cos(3\varphi_{el}) \right). \tag{36}$$

3.2.2. Switching Losses

Calculation of the switching losses is carried out in the same manner as the conduction losses for the IGBT and diode pair T_1, D_2 . The switching losses of the IGBT occur during the transition from blocking to conducting state and vice versa. For the diode, the switching

losses are mainly related to the reverse recovery effect during the transition from conduction to blocking state. The energies for one switching event are given in the corresponding semiconductor data sheet, as outlined in Figure 10, for the used module. In [46,49,51], a linear dependence between the switching energy $w_{sw,lin}$ and the actual phase current i_U , in the form

$$w_{sw,lin} = k_{sw,T,D} \cdot i_U(\varphi_{el}) \tag{37}$$

is assumed. However, as depicted in Figure 10, neither the diode nor the IGBT behave linearly regarding their switching losses. Thus, a second-order polynomial equation of the form

$$\tilde{w}_{Eon,T_1} = a_{Eon} \cdot i_U + b_{Eon} \cdot i_U^2 + c_{Eon} \tag{38}$$

$$\tilde{w}_{Eoff,T_1} = a_{Eoff} \cdot i_U + b_{Eoff} \cdot i_U^2 + c_{Eoff} \tag{39}$$

$$\tilde{w}_{Err,D_2} = a_{Err} \cdot i_U + b_{Err} \cdot i_U^2 + c_{Err} \tag{40}$$

is used to model the nonlinear behavior of the turn-on and turn-off energies \tilde{w}_{Eon,T_1} , \tilde{w}_{Eoff,T_1} of the IGBT and for the diode reverse recovery losses \tilde{w}_{Err,D_2} . The used sine modulation scheme causes each semiconductor to switch once in each PWM duty cycle. Therefore, a linear relationship between the switching frequency f_s and the switching power losses

$$\tilde{p}_{Eon,T_1} = \tilde{w}_{Eon,T_1}(\varphi_{el}) \cdot f_s \tag{41}$$

$$\tilde{p}_{Eoff,T_1} = \tilde{w}_{Eoff,T_1}(\varphi_{el}) \cdot f_s \tag{42}$$

$$\tilde{p}_{Err,D_2} = \tilde{w}_{Err,D_2}(\varphi_{el}) \cdot f_s \tag{43}$$

exists.

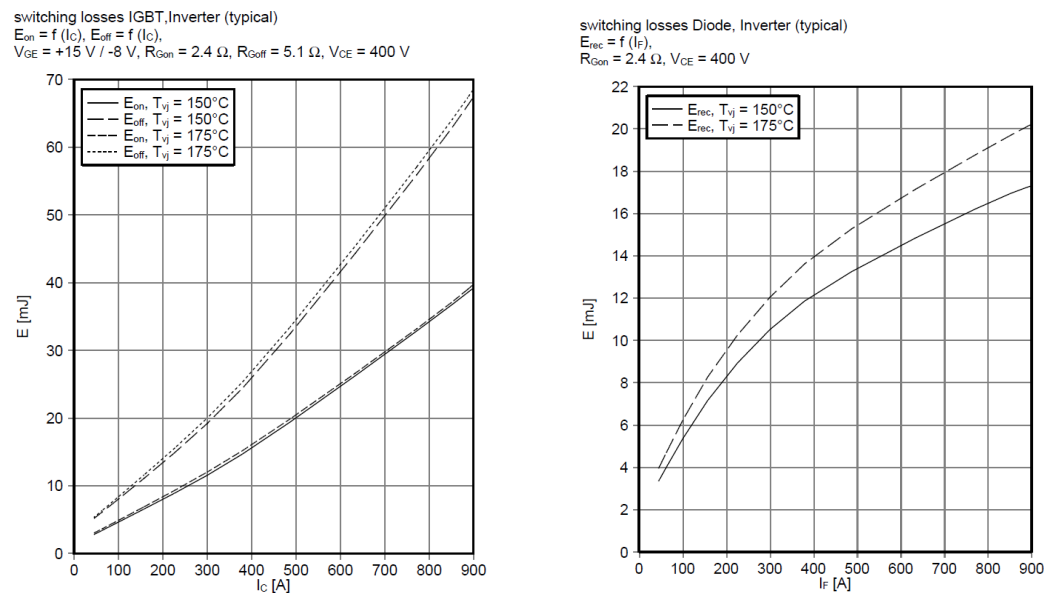


Figure 10. Switching energies with respect to the load current of the used IGBT module [50].

In addition to the polynomial fit, the temperature dependencies of the switching losses are also taken into account. Furthermore, the switching losses behave nonlinearly regarding the applied blocking voltage, which is in case of the VSI the DC-voltage u_{DC} . Averaging

the switching losses over one fundamental wave period and including the aforementioned temperature and blocking voltage dependencies leads to

$$P_{Eon,T_1} = f_s \left(\frac{u_{DC}}{u_{ref,T}} \right)^{\kappa_T} \left(1 + \alpha_T(\vartheta_{j,T} - \vartheta_{ref,T}) \right) \left(\frac{c_{Eon}}{2} + \frac{a_{Eon} \hat{I}_N}{\pi} + \frac{b_{Eon} \hat{I}_N^2}{4} \right) \quad (44)$$

$$P_{Eoff,T_1} = f_s \left(\frac{u_{DC}}{u_{ref,T}} \right)^{\kappa_T} \left(1 + \alpha_T(\vartheta_{j,T} - \vartheta_{ref,T}) \right) \left(\frac{c_{Eoff}}{2} + \frac{a_{Eoff} \hat{I}_N}{\pi} + \frac{b_{Eoff} \hat{I}_N^2}{4} \right) \quad (45)$$

$$P_{Err,D_2} = f_s \left(\frac{u_{DC}}{u_{ref,D}} \right)^{\kappa_D} \left(1 + \alpha_D(\vartheta_{j,D} - \vartheta_{ref,D}) \right) \left(\frac{c_{Err}}{2} + \frac{a_{Err} \hat{I}_N}{\pi} + \frac{b_{Err} \hat{I}_N^2}{4} \right) \quad (46)$$

describing the averaged switching losses with respect to the amplitude of the applied phase current \hat{I}_N , the actual junction temperatures of the IGBT $\vartheta_{j,T}$ and the diode $\vartheta_{j,D}$ and the applied DC-voltage u_{DC} . The voltages $u_{ref,T}$ and $u_{ref,D}$ describe the specific working point voltage in the semiconductor data sheet for which the switching losses are measured. The exponents κ_T and κ_D express the nonlinear behavior of the blocking voltage to the switching losses.

For the proposed VSI with six IGBT and diode pairs, the overall power losses of the inverter can be calculated as

$$P_{inv} = 6 \left(P_{c,T_1} + P_{c,D_2} + P_{Eon,T_1} + P_{Eoff,T_1} + P_{Err,D_2} \right). \quad (47)$$

3.2.3. Thermal Model

The thermal model of the water-cooled IGBT module is mainly defined by the thermal paths conducting heat from each IGBT and each diode to the cooling circuit. In the proposed thermal model, as outlined in Figure 11, cross-coupling effects between each semiconductor on the module are neglected. As the IGBTs and the diodes are loaded equally, the power losses $P_{v,T}$ and $P_{v,D}$ can be combined for all six semiconductors, leading to two heat dissipation sources. The heat is transferred to the cooling circuit by the thermal resistance $R_{th_{jw},T}$ from the IGBT and by the thermal resistance $R_{th_{jw},D}$ from the diode. The main advantage of equivalent circuit diagram models is the ease of parameterization of the models using the thermal impedances directly given in the data sheet [50]. Using the proposed model, the junction temperature of the semiconductors $\vartheta_{j,T}$ and $\vartheta_{j,D}$ can be calculated with

$$\vartheta_{j,T} = P_{v,T} \frac{R_{th_{jw},T}}{6} + \vartheta_{wg} \quad (48)$$

for the IGBTs and with

$$\vartheta_{j,D} = P_{v,D} \frac{R_{th_{jw},D}}{6} + \vartheta_{wg} \quad (49)$$

for the diodes, where ϑ_{wg} denotes the temperature of the coolant. If channel flow characteristics [52] are assumed for the flow of the liquid coolant, the relation between the power dissipation of the semiconductors $P_{v,T}$, $P_{v,D}$, the coolant inlet and outlet temperatures ϑ_{in} , ϑ_{out} and a given flow rate \dot{V}_{wg} can be expressed by

$$P_{v,T} + P_{v,D} = \rho_{wg}(\vartheta_{wg}) \dot{V}_{wg} c_{p,wg}(\vartheta_{wg}) (\vartheta_{out} - \vartheta_{in}). \quad (50)$$

Due to the expected minor temperature increase between the inlet and outlet temperatures, the coolant temperature is assumed to be

$$\vartheta_{wg} = \frac{\vartheta_{wg,in} + \vartheta_{wg,out}}{2}. \quad (51)$$

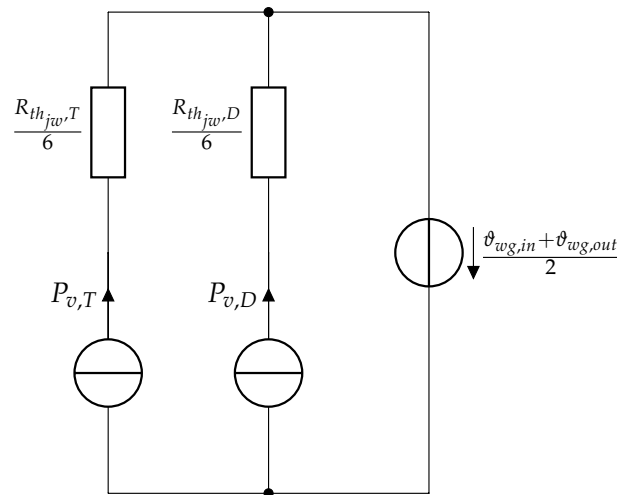


Figure 11. IGBT thermal equivalent circuit model.

3.3. EM Model

Modeling the permanent magnet synchronous machine (PMSM) is carried out using a fundamental wave model in d, q coordinates with saturation effects, as outlined in [53]. Furthermore, the model is expanded by nonlinear iron losses ζ_d and ζ_q introduced in [54]. As the time constant of the electrical drive is significantly smaller, in comparison to that of the mechanical system, the current dynamics in the model are neglected. This lead to the equivalent circuit models outlined in Figure 12 and the stationary machine equations [54]

$$u_d = (R_s + \zeta_q L_d) i_d - \omega_{el} L_q i_q + \zeta_q \Psi_{pm} \tag{52}$$

$$u_q = (R_s + \zeta_d L_q) i_q + \omega_{el} L_d i_d + \omega_{el} \Psi_{pm} \tag{53}$$

describing the electrical behavior of the drive in d, q coordinates. For the sake of simplicity and a better readability, the parameter dependencies are only outlined in the equivalent circuit model and not in the equations. As can be seen the parameters L_d, L_q and Ψ_{pm} depend on the actual current working point i_{d0}, i_{q0} of the machine and caused by the saturation of the electrical drive. They were identified experimentally on a drive test-bench and are outlined in Figure 13. The dependencies of the iron losses ζ_d and ζ_q on the torque M_{em} and the velocity ω_{el} are shown in Figure 14. Furthermore, the copper resistance R_s depends on the stator temperature ϑ_{st} , which can be described by

$$R_s = R_{s,\vartheta_0} [1 + \alpha_{cu,\vartheta_0} (\vartheta_{st} - \vartheta_{cu,0})], \tag{54}$$

where α_{cu,ϑ_0} is the temperature coefficient of copper and R_{s,ϑ_0} is the reference resistance at the reference temperature $\vartheta_{cu,0}$. The magnetic flux depends on the rotor temperature ϑ_{ro} and can be described by

$$\Psi_{pm} = \Psi_{pm,\vartheta_0} [1 + \alpha_{pm,\vartheta_0} (\vartheta_{ro} - \vartheta_{pm,0})], \tag{55}$$

where α_{pm,ϑ_0} is the temperature coefficient of the permanent magnet material and Ψ_{pm,ϑ_0} describes the reference magnetic flux at the reference temperature $\vartheta_{pm,0}$. The link between the electrical model and the corresponding air gap torque M_{air} , taking the iron losses into account, can be described by [55]

$$M_{air} = \frac{3}{2} p [\Psi_{pm} (i_q - u_q \frac{\zeta_q}{\omega_{el}^2 L_q}) + (L_d - L_q) (i_d - u_d \frac{\zeta_d}{\omega_{el}^2 L_d}) (i_q - u_q \frac{\zeta_q}{\omega_{el}^2 L_q})], \tag{56}$$

with p denoting the number of pole pairs.

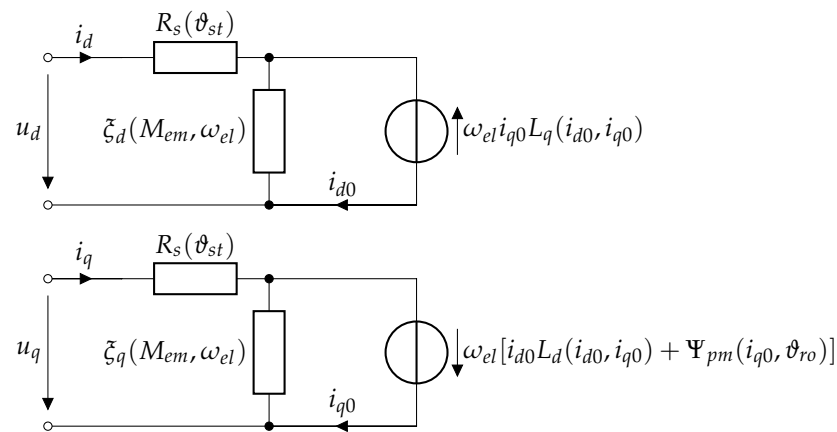


Figure 12. Saturation- and iron loss-dependent PMSM equivalent circuits.

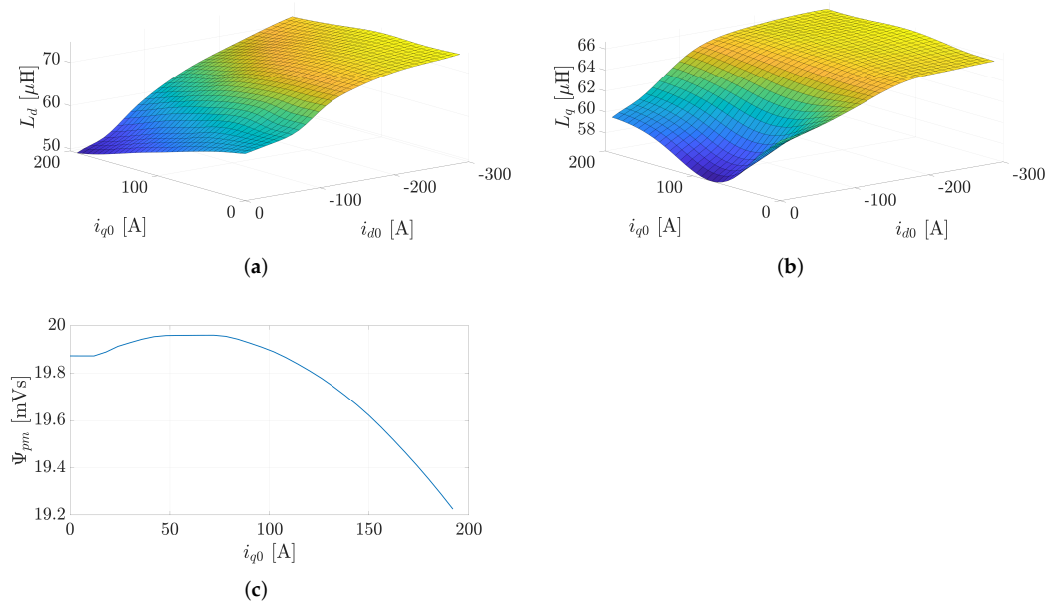


Figure 13. Working point-dependent drive parameters (a) Direct inductance L_d , (b) Quadrature inductance L_q , (c) Magnetic flux Ψ_{pm} .

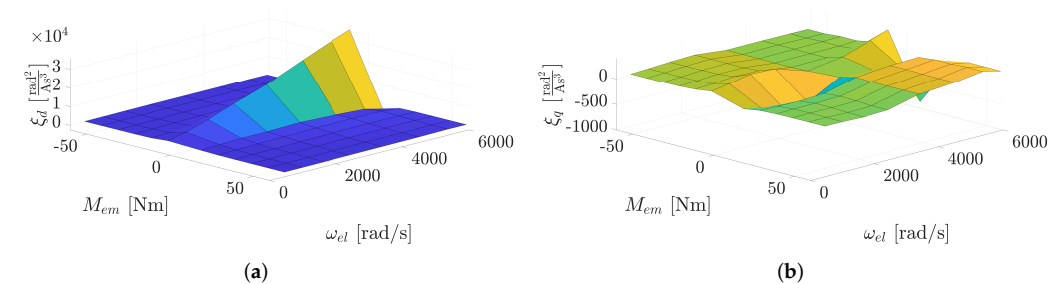


Figure 14. Working point-dependent iron losses (a) Direct axis iron loss parameter ξ_d , (b) Quadrature axis iron loss parameter ξ_q .

3.4. Environment Model

In order to use realistic driving scenarios for the vehicle defined in the previous sections, four different drive cycles were defined, which represent typical daily commuter routes to work in the urban and inter-urban areas around the German city Trier and

are outlined in Figures 15 and 16. The environment model describes the required route parameters of the driven route, including

- Legal speed limit;
- Curve radii;
- Road slope and elevation.

The presented data were extracted from the HERE map database [56] for the given GPX tracks.

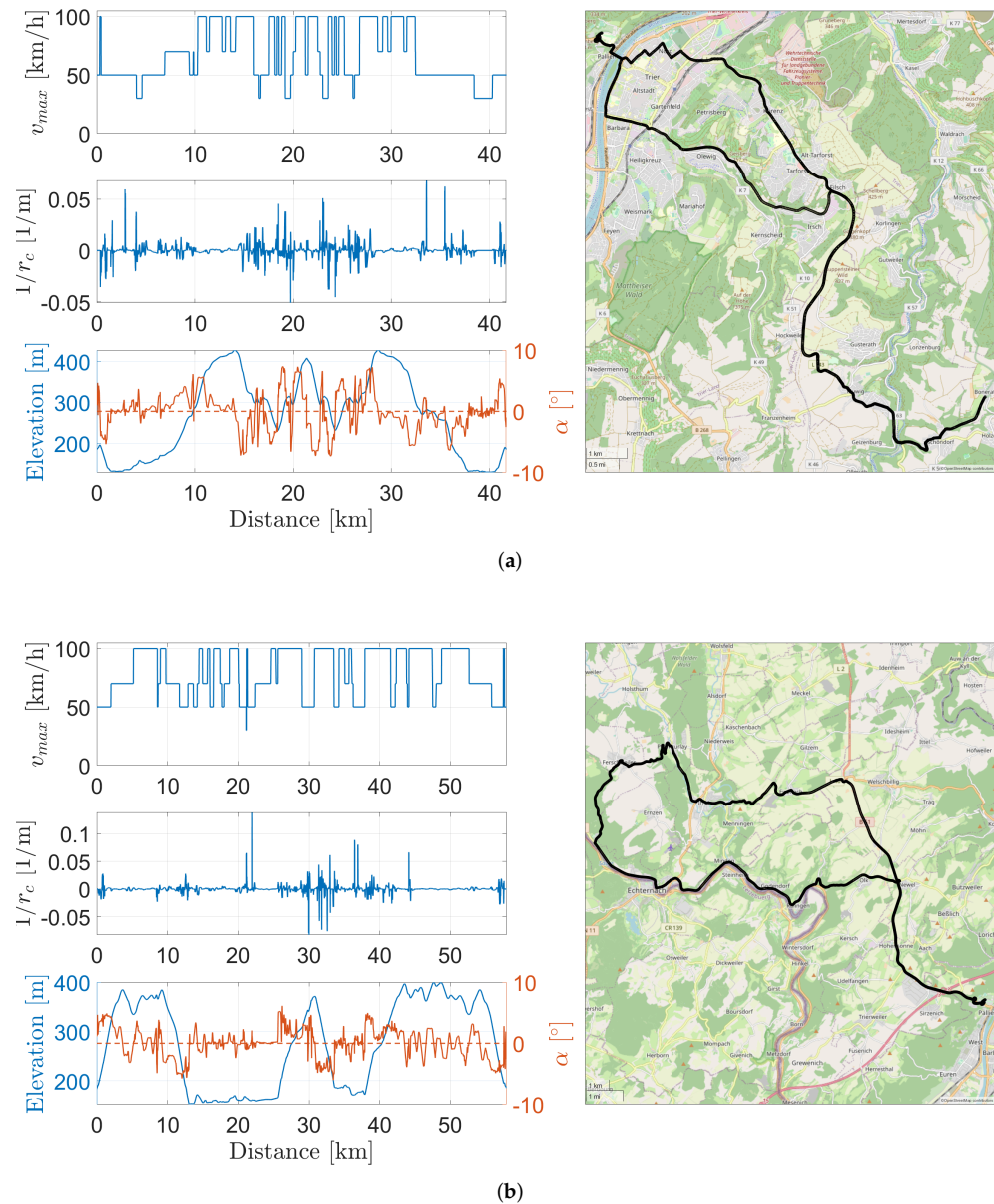


Figure 15. Drive cycle overview (a) Drive cycle 1, (b) Drive cycle 2.

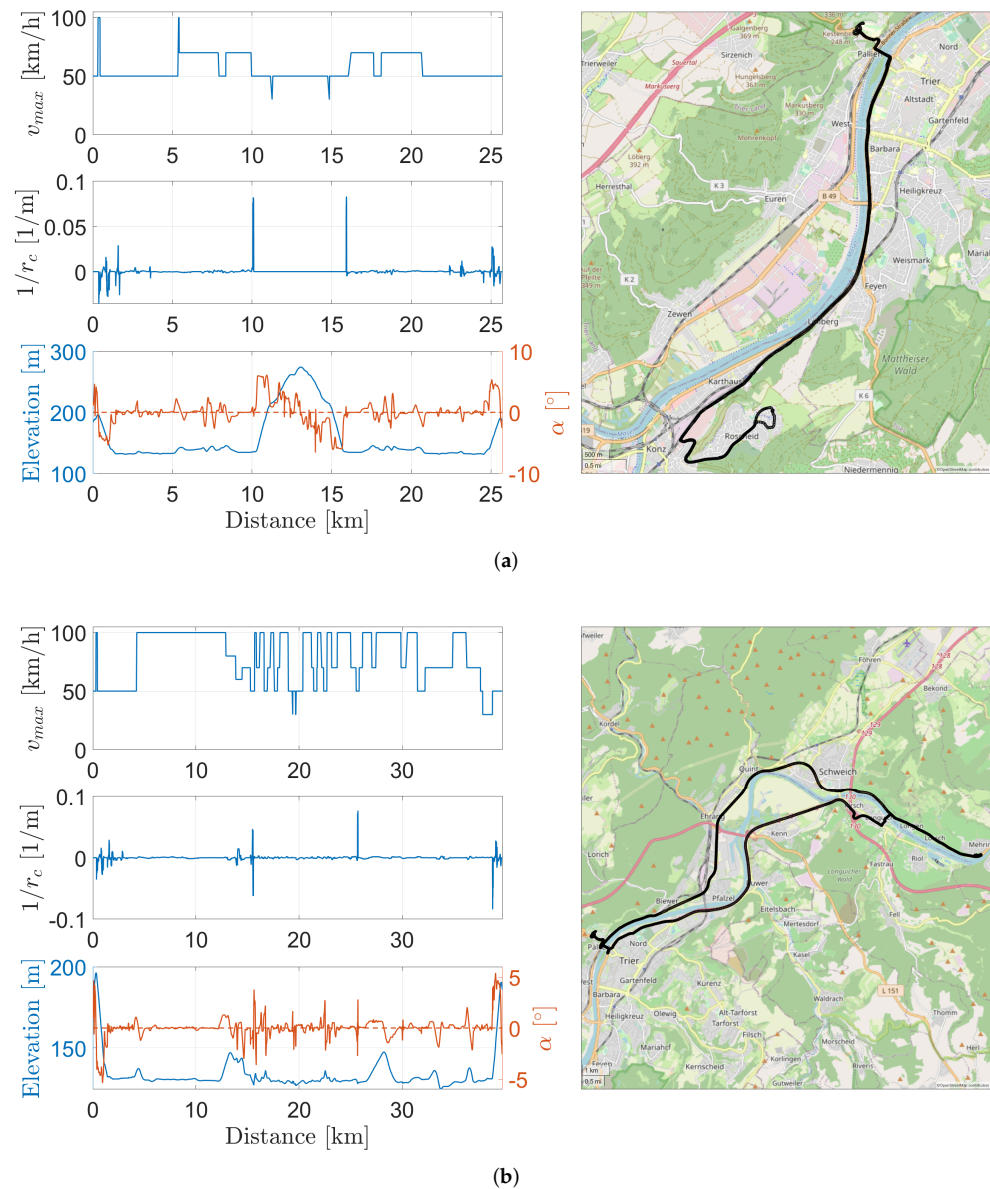


Figure 16. Drive cycle overview (a) Drive cycle 3, (b) Drive cycle 4.

To account for the influence of commuting distances, all selected routes are of different length. Furthermore, it can be seen that the elevation profile is more distinct for drive cycles 1 and 2 than for drive cycles 3 and 4, thus covering the influence of different elevation profiles. Furthermore, the speed profiles of the drive cycles are also different. As can be seen, the legal speed limit v_{max} for the drive cycles 1–3 is slower than that for drive cycle 4. It is important to mention that the start and end points of the route are at the same altitude. This avoids the insertion or extraction of potential energy of the system and thus, falsification of the results of the proposed sensitivity analysis.

4. Longitudinal Economic MPC

In the following, the longitudinal economic model predictive controller (EMPC) used to control the BEV is presented. Modern energy-efficient longitudinal motion controllers use information about the environment, such as route data [4]. Normally, the route information is provided by the map data provider as a function of the vehicle position. To process the

data directly in the prediction, the proposed controller is discretized over position, rather than time. The domain change is performed using the relation [4,57]

$$\frac{d}{dt} = \frac{d}{ds} \frac{ds}{dt} = \frac{d}{ds} v. \tag{57}$$

Given the longitudinal motion model described in (A1)–(A9) and the transformation in (57), the velocity of the vehicle can be expressed as

$$\frac{d}{ds} v_{ego} = \frac{M_{em} \frac{i_g}{r_w} - c_r m_v g \cos(\alpha) - m_v g \sin(\alpha) - \frac{1}{2} \rho_{air} c_w A v_{ego}^2}{m_{eq} v_{ego}}, \tag{58}$$

as the first state of the controller design. The battery energy E_b is used as the second state, which is given by

$$\frac{d}{ds} E_b = \frac{U_{ocv} i_b n_{cell}}{v_{ego}}. \tag{59}$$

Here, the open circuit voltage U_{ocv} is assumed to be constant during the prediction. The battery current i_b can be determined using

$$P_{DC}(M_{em}, v_{ego}) + P_{pto} = i_b n_{cell} (U_{ocv} - u_{RC1} - i_b R_s), \tag{60}$$

where $P_{DC}(M_{em}, v_{ego})$ denotes the DC power requested by the inverters and P_{pto} outlines the power needed by auxiliary consumers. This leads to

$$i_b = \frac{n_{cell}(U_{ocv} - u_{RC1})}{2R_s n_{cell}} - \frac{\sqrt{-n_{cell}(n_{cell}(u_{RC1} U_{ocv} - u_{RC1}^2 - u_{ocv}^2) + 4R_s(P_{pto} + P_{DC}(M_{em}, v_{ego})))}}{2R_s n_{cell}} \tag{61}$$

for the battery current. To ensure real-time capability and thus, practical applicability of the controller, the complex and nonlinear behavior of the drive and inverter is not transferred directly into the controller, as this would result in an overly complex controller design. Therefore, the DC power, as outlined in Figure 17a, is approximated using a second-order polynomial of the form

$$P_{DC}(M_{em}, v_{ego}) \approx 227.2 - 1.12M_{em} + 60.04v_{ego} + 0.3696M_{em}^2 + 20.67v_{ego}M_{em} + 1.206v_{ego}^2. \tag{62}$$

the voltage drop u_{RC1} is calculated by

$$\frac{d}{ds} u_{RC1} = \frac{\frac{i_b}{C_1} - \frac{u_{R1}}{C_1 R_1}}{v_{ego}} \tag{63}$$

and serves as the third system state for the controller design. As outlined in Section 3.1.1 the parameters R_1 and C_1 are dependent on the working point. Nevertheless, the parameters are assumed to be constant over the prediction horizon as the working point, especially as the battery temperature and SoC, change only slowly. To keep the controller simple, only the dominant RC element of the battery is considered.

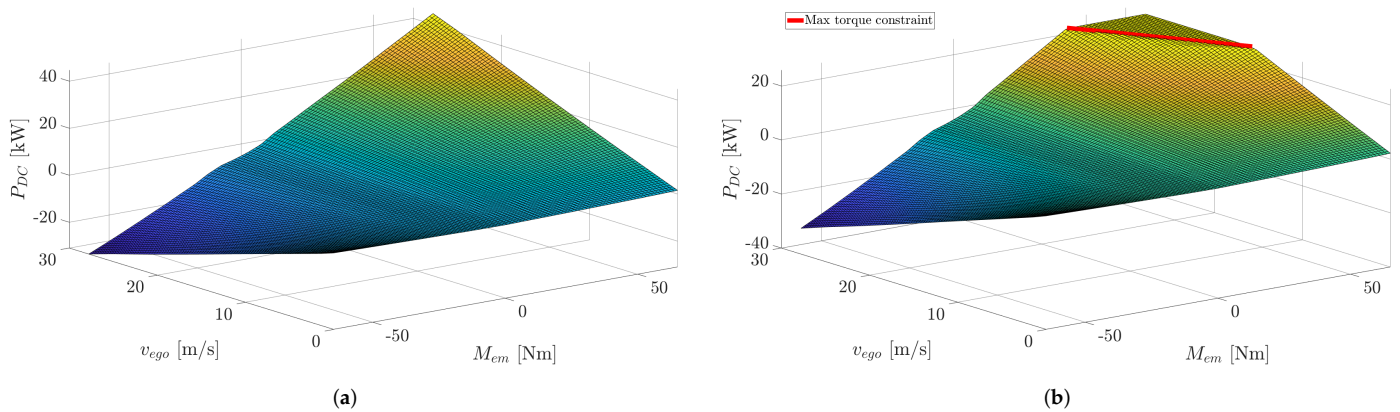


Figure 17. DC power map (a) without battery current limitation, (b) with battery current limitation.

According to (58)–(63), the nonlinear state space model can then be fully described by

$$\frac{d}{ds} \begin{bmatrix} v_{ego} \\ E_b \\ u_{RC1} \end{bmatrix} = \begin{bmatrix} \frac{M_{em} \frac{i_g}{r_w} - c_r m_v g \cos(\alpha) - m_v g \sin(\alpha) - \frac{1}{2} \rho_{air} c_w A v_{ego}^2}{m_{eq} v_{ego}} \\ \frac{U_{ocv} i_b n_{cell}}{v_{ego} u_{R1}} \\ \frac{i_b}{C_1} - \frac{C_1 R_1}{v_{ego}} \end{bmatrix}, \quad (64)$$

with

$$\mathbf{u} = M_{em} \quad (65)$$

as the model input.

The energy efficiency control objective of the economic cost function

$$J(\mathbf{x}, \mathbf{u}) = \int_0^{S_p} [a_c \cdot (v_{ego}(s) - v_{ref})^2 + b_c \cdot (M_{em}(s) - M_{ref})^2] ds + c_c \cdot E_b(S_p) + d_c \cdot (v_{ego}(S_p) - v_{ref})^2 \quad (66)$$

is defined by the penalization c_c of the utilized battery energy E_b at the end of the prediction horizon S_p within the Mayer term. However, considering only the battery energy would result in an unacceptable increase in driving time, due to the forced energy savings. To prevent this, the deviation from the reference velocity v_{ref} is penalized in the Mayer and Lagrange term. Furthermore, the deviation of the manipulated variable M_{em} to the required reference torque M_{ref} is penalized, in order to smoothen the controller response.

The maximum possible input torque $M_{em} \in [M_{min}, M_{max}]$ is treated as a linear constraint. Furthermore, the power limitation caused by the maximum battery current, which results in a torque envelope for positive torques, as outlined in Figure 17b, is considered as a linear constraint of the form

$$M_{em} \leq 97.01 - 2.173 v_{ego}. \quad (67)$$

Furthermore, the optimization problem should be bounded to ensure solvability and stability [58], which can be ensured by adding the constraints

$$\begin{bmatrix} 5 \\ -300000 \\ -50 \end{bmatrix} \leq \mathbf{x}(s) \leq \begin{bmatrix} 30 \\ 300000 \\ 50 \end{bmatrix} \quad \text{with } s \in [0, S_p] \quad (68)$$

to the optimization problem.

Equations (64)–(68) lead to the optimization problem

$$\min_{\mathbf{u}} \quad J(\mathbf{x}, \mathbf{u}) \tag{69}$$

$$\text{s.t.} \quad \frac{d}{ds} \mathbf{x} = f(\mathbf{x}, \mathbf{u}) \tag{70}$$

$$\mathbf{x}(0) = \mathbf{x}_0 \tag{71}$$

$$M_{min} \leq M_{em}(s) \leq M_{max} \quad s \in [0, S_p] \tag{72}$$

$$M_{em}(s) \leq 97.01 - 2.173v_{ego}(s) \quad s \in [0, S_p] \tag{73}$$

$$\begin{bmatrix} 5 \\ -300000 \\ -50 \end{bmatrix} \leq \mathbf{x}(s) \leq \begin{bmatrix} 30 \\ 300000 \\ 50 \end{bmatrix} \quad s \in [0, S_p], \tag{74}$$

which is discretized using a fourth-order Runge–Kutta algorithm and computed with the open-source framework acados [59].

The reference velocity v_{ref} is subject to two conditions. First, the maximum allowed legal speed v_{max} , as already outlined in Figure 15, needs to be taken into account. Second, the maximum lateral acceleration $a_{l,max}$ allowed when driving a curve with the curve radius c_r results also in a speed limit, which is defined by

$$v_{l,max} = \sqrt{r_c \cdot a_{l,max}}. \tag{75}$$

The minimum of these two conditions would lead to the reference velocity v_{ref} . However, taking only the minimum may cause discontinuities to appear in the reference trajectory. To smoothen the reference trajectory, the discrete optimization problem [60]

$$\min_{\mathbf{v}_{smooth}} \quad \sum_{i=1}^{N_p} (v_{ref}(k+i|k) - v_{smooth}(k+i|k))^2 \tag{76}$$

$$\text{s.t.} \quad v_{smooth}(k+i+1|k) - v_{smooth}(k+i|k) \leq r_{max} \quad \forall i \in \{1, 2, \dots, N_p\} \tag{77}$$

$$v_{smooth}(k+i|k) \leq v_{ref}(k+i|k) \quad \forall i \in \{1, 2, \dots, N_p\}, \tag{78}$$

with r_{max} as the maximum allowed change of the optimization variable, is used over the prediction horizon N_p .

5. Sensitivity Setup

To perform a suitable sensitivity analysis, the sensitivity setup needs to be defined, including the following information:

- Which parameters are investigated;
- The injection point of each parameter;
- The distribution underlying each parameter;
- The model outputs of interest.

For the proposed sensitivity analysis in this article, all investigated parameters are outlined in Table 1. They are arranged into groups, according to the components to which they belong. For the vehicle itself and its powertrain components, each parameter belongs to the parameters of the proposed models of Section 3. How the distributions are injected into the model and the types of error are also outlined in Table 1. Relative errors represent a percentage deviation of the nominal model values, whereas absolute errors directly describe the deviation of the parameter itself. The standard deviation σ for normally distributed parameters is mostly defined using the 3σ values, representing the maximum error of the addressed parameter. As the objective of this investigation is to quantify the influences of the proposed parameters on the energy efficiency the outputs of interest are the combined power losses of all powertrain devices P_l and the consumed battery energy E_b . The combined power losses P_l consider the battery, inverter, electric drive and gearbox

losses. As the energy consumption of the vehicle is also influenced by the average driving speed, the required driving time t_d , as an indicator of the average driving speed, is also taken into account.

Table 1. Distributions of parameters for sensitivity analysis.

	Name	Description	Type of Error	Distribution	Parameter	Values	Units
Battery	$e_{R_s,b}$	Deviation of series resistance R_s	relative	Normal	μ, σ	0, 0.05/3	—
	e_{C_1}	Deviation of capacitance C_1	relative	Normal	μ, σ	0, 0.05/3	—
	e_{R_1}	Deviation of resistance R_1	relative	Normal	μ, σ	0, 0.05/3	—
	e_{C_2}	Deviation of capacitance C_2	relative	Normal	μ, σ	0, 0.05/3	—
	e_{R_2}	Deviation of resistance R_2	relative	Normal	μ, σ	0, 0.05/3	—
	$e_{U_{ocv}}$	Deviation of open circuit voltage	relative	Normal	μ, σ	0, 0.025/3	—
	θ_b	Variation of start temperature	absolute	Uniform	a, b	20, 40	°C
	R_{thca}	Variation of thermal resistance R_{thca}	absolute	Normal	μ, σ	2.6042, 0.1302/3	Ω
	R_{thct}	Variation of thermal resistance R_{thct}	absolute	Normal	μ, σ	0.3682, 0.0184/3	Ω
	R_{thta}	Variation of thermal resistance R_{thta}	absolute	Normal	μ, σ	1.0526, 0.0526/3	Ω
	C_c	Variation of thermal capacitance C_c	absolute	Normal	μ, σ	2544.2, 127.21/3	F
C_t	Variation of thermal capacitance C_t	absolute	Normal	μ, σ	8.072, 3.4036/3	F	
Inverter	e_{a_i}	Deviation of forward characteristics IGBT	relative	Normal	μ, σ	0, 0.02/3	—
	e_{b_i}	Deviation of forward characteristics IGBT	relative	Normal	μ, σ	0, 0.02/3	—
	e_{a_d}	Deviation of forward characteristics diode	relative	Normal	μ, σ	0, 0.02/3	—
	e_{b_d}	Deviation of forward characteristics diode	relative	Normal	μ, σ	0, 0.02/3	—
	$e_{a_{Err}}$	Deviation of reverse recovery characteristics diode	relative	Normal	μ, σ	0, 0.02/3	—
	$e_{b_{Err}}$	Deviation of reverse recovery characteristics diode	relative	Normal	μ, σ	0, 0.02/3	—
	$e_{c_{Err}}$	Deviation of reverse recovery characteristics diode	relative	Normal	μ, σ	0, 0.02/3	—
	$e_{a_{Eon}}$	Deviation of turn on losses IGBT	relative	Normal	μ, σ	0, 0.02/3	—
	$e_{b_{Eon}}$	Deviation of turn on losses IGBT	relative	Normal	μ, σ	0, 0.02/3	—
	$e_{c_{Eon}}$	Deviation of turn on losses IGBT	relative	Normal	μ, σ	0, 0.02/3	—
	$e_{a_{Eoff}}$	Deviation of turn off losses IGBT	relative	Normal	μ, σ	0, 0.02/3	—
$e_{b_{Eoff}}$	Deviation of turn off losses IGBT	relative	Normal	μ, σ	0, 0.02/3	—	
$e_{c_{Eoff}}$	Deviation of turn off losses IGBT	relative	Normal	μ, σ	0, 0.02/3	—	
	$\theta_{w,in}$	Variation of water inlet temperature	absolute	Uniform	a, b	0, 50	°C
Drive	$e_{R_s,EM}$	Deviation of winding resistance R_s	relative	Normal	μ, σ	0, 0.03/3	—
	e_{L_d}	Deviation of direct inductance L_d	relative	Normal	μ, σ	0, 0.0133/3	—
	e_{L_q}	Deviation of quadrature inductance L_q	relative	Normal	μ, σ	0, 0.015/3	—
	$e_{\Psi_{pm}}$	Deviation of magnetic flux Ψ_{pm}	relative	Normal	μ, σ	0, 0.025/3	—
	e_{ζ_q}	Deviation of quadrature iron losses ζ_q	relative	Normal	μ, σ	0, 0.02/3	—
	e_{ζ_d}	Deviation of direct iron losses ζ_d	relative	Normal	μ, σ	0, 0.02/3	—
	θ_{ro}	Variation of rotor temperature θ_{ro}	absolute	Uniform	a, b	40, 80	°C
	θ_{st}	Variation of stator temperature θ_{st}	absolute	Uniform	a, b	40, 80	°C
Vehicle	m_v	Variation of the vehicle mass	absolute	Birnbaum–Saunders	β, γ	652.111, 0.0742427	kg
	P_{pto}	Variation of auxiliary consumers	absolute	Uniform	a, b	250, 750	W
	θ_a	Variation of ambient temperature	absolute	Normal	μ, σ	12.261, 8.52975	°C
	p_{air}	Variation of ambient pressure	absolute	Normal	μ, σ	98427.7, 843.09	Pa
	c_r	Variation of rolling resistance	absolute	Uniform	a, b	0.01, 0.015	—
Controller	c_c	Energy related cost function parameter	absolute	Uniform	a, b	0, 6	—
	$\theta_{a,mpc}$	Error of ambient temperature measurement	absolute	Normal	μ, σ	12.261, 8.52975	°C
	$p_{air,mpc}$	Error of air pressure estimation	absolute	Normal	μ, σ	98427.7, 843.09	Pa
	$c_{r,mpc}$	Error of rolling resistance estimation	absolute	Uniform	a, b	0.01, 0.015	—
	$m_{v,mpc}$	Error of vehicle mass estimation	absolute	Birnbaum–Saunders	β, γ	652.111, 0.0742427	kg
	$e_{U_{ocv},mpc}$	Error of open circuit voltage estimation	relative	Normal	μ, σ	0, 0.05/3	—
	$e_{R_s,mpc}$	Error of battery series resistance estimation	relative	Normal	μ, σ	0, 0.05/3	—
	$e_{R_1,mpc}$	Error of battery RC-resistance estimation	relative	Normal	μ, σ	0, 0.05/3	—
	$e_{C_1,mpc}$	Error of battery RC-capacitance estimation	relative	Normal	μ, σ	0, 0.05/3	—
	$e_{\alpha,mpc}$	Error of slope measurement	relative	Normal	μ, σ	0, 0.05/3	—
	$e_{P_{pto},mpc}$	Error of auxiliary power estimation	absolute	Uniform	a, b	250, 750	W
	$e_{c_{r,mpc}}$	Error of curvature measurement	relative	Normal	μ, σ	0, 0.05/3	—
	$e_{SoC,mpc}$	Error of SoC estimation	relative	Normal	μ, σ	0, 0.10/3	—
	$e_{\theta_b,mpc}$	Error of battery temperature estimation	relative	Normal	μ, σ	0, 0.05/3	—
	$e_{I_b,mpc}$	Error of battery current measurement	relative	Normal	μ, σ	0, 0.05/3	—

The first step is to conduct a Morris screening of the proposed model, controller and parameter setup. Afterwards, the results provided by the Morris screening are used to exclude unimportant parameters from the quantitative sensitivity analysis, in order to reduce the computational time of the Monte-Carlo setup. The results of the proposed sensitivity analysis are outlined in the following chapter.

6. Simulation Results

In this chapter, the results of the sensitivity analysis are discussed. In Section 6.1, the results of the Morris screening are presented while, in Section 6.2, the outcomes of the quantitative variance-based sensitivity analysis are discussed.

6.1. Morris Screening

The results of the Morris screening for the four different drive cycles are outlined in Figures 18–21. In general, it can be seen that the required battery energy E_b behaves more linearly than the power losses P_l throughout all driving cycles, as $\sigma \ll \mu^*$ holds. As σ is not negligibly small, compared to μ^* , for the parameter dependencies of the power losses P_l , nonlinear interactions between parameters can be assumed. Furthermore, it can be seen for both outputs E_b and P_l , that only a small subset of parameters have high values of μ^* or σ compared to the rest of the parameters. Consequently only these parameters are taken into account in the variance-based sensitivity analysis. The remaining parameter set is outlined in Table 2.

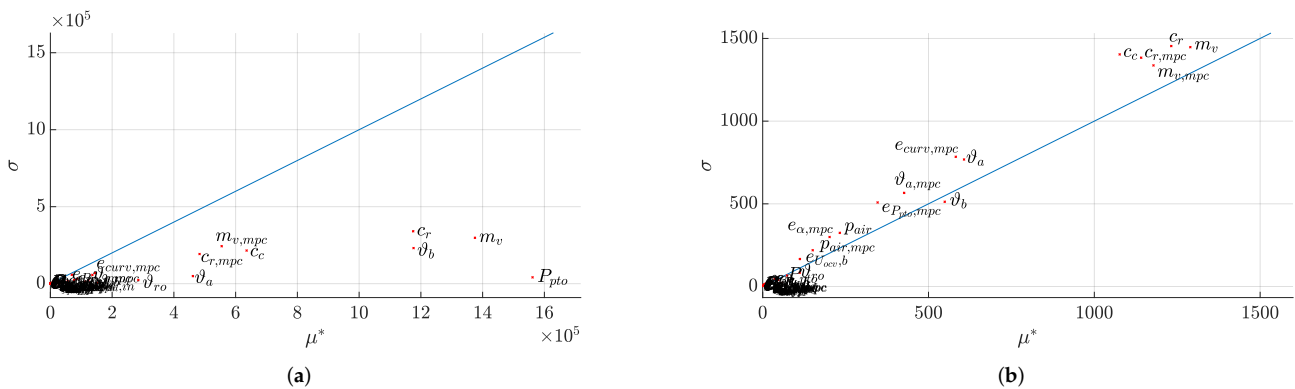


Figure 18. Morris screening for drive cycle 1 (a) Bat energy E_b , (b) Power losses P_l .

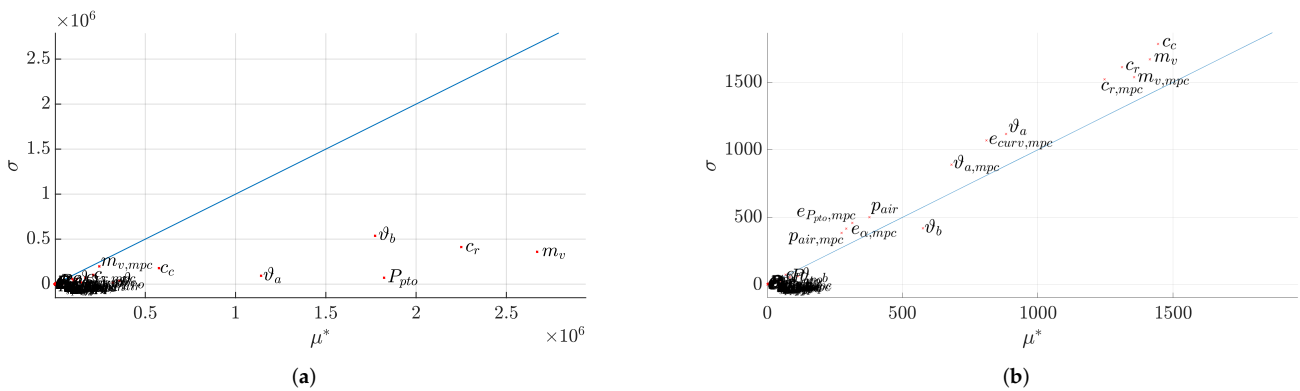


Figure 19. Morris screening for drive cycle 2 (a) Bat energy E_b , (b) Power losses P_l .

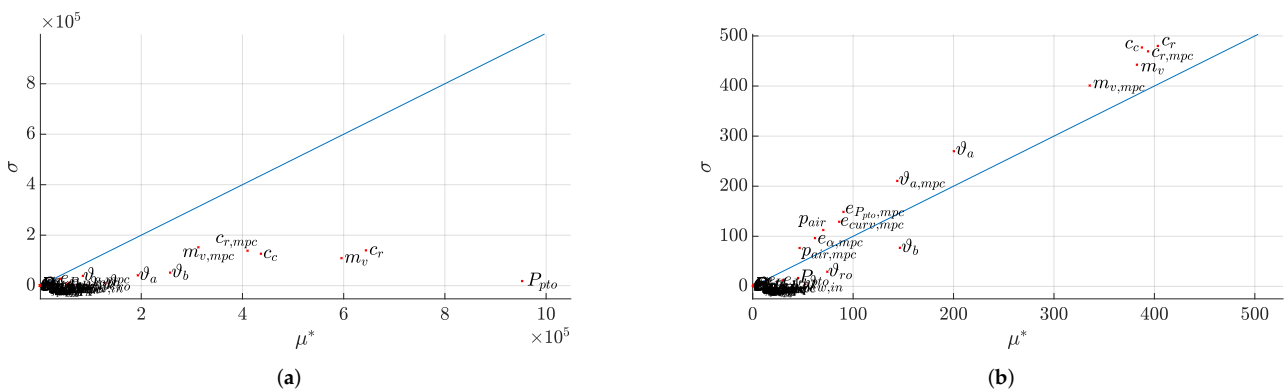


Figure 20. Morris screening for drive cycle 3 (a) Bat energy E_b , (b) Power losses P_l .

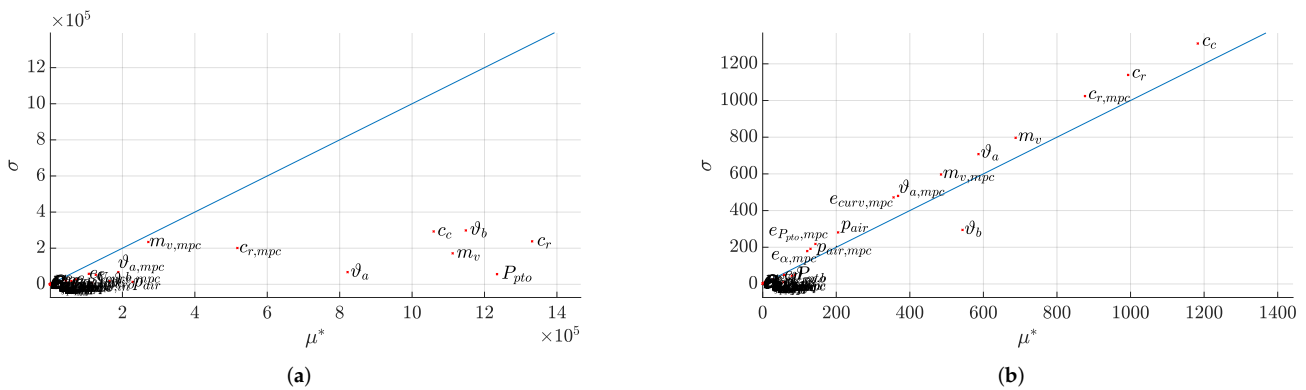


Figure 21. Morris screening for drive cycle 4 (a) Bat energy E_b , (b) Power losses P_l .

Table 2. Reduced parameter set for the variance-based sensitivity analysis.

	Name	Description	Type of Error	Distribution	Parameter	Values	Units
Battery	ϑ_b	Variation of start temperature	absolute	Uniform	a, b	20, 40	°C
Inverter	$\vartheta_{w,in}$	Variation of water inlet temperature	absolute	Uniform	a, b	0, 50	°C
Drive	ϑ_{ro}	Variation of rotor temperature ϑ_{ro}	absolute	Uniform	a, b	40, 80	°C
Vehicle	m_v	Variation of the vehicle mass	absolute	Birnbaum–Saunders	β, γ	652.111, 0.0742427	kg
	P_{pto}	Variation of auxiliary consumers	absolute	Uniform	a, b	250, 750	W
	ϑ_a	Variation of ambient temperature	absolute	Normal	μ, σ	12.261, 8.52975	°C
	c_r	Variation of rolling resistance	absolute	Uniform	a, b	0.01, 0.015	–
Controller	c_c	Energy related cost function parameter	absolute	Uniform	a, b	0, 6	-
	$\vartheta_{a,mpc}$	Error of ambient temperature measurement	absolute	Normal	μ, σ	12.261, 8.52975	°C
	$c_{r,mpc}$	Error of rolling resistance estimation	absolute	Uniform	a, b	0.01, 0.015	–
	$m_{v,mpc}$	Error of vehicle mass estimation	absolute	Birnbaum–Saunders	β, γ	652.111, 0.0742427	kg
	$e_{P_{pto,mpc}}$	Error of auxiliary power estimation	absolute	Uniform	a, b	250, 750	W
	$e_{curv,mpc}$	Error of curvature measurement	relative	Normal	μ, σ	0, 0.05/3	–

6.2. Sobol Indices

Figure 22a outlines the histograms of the required battery energy E_b , caused by the parameter distributions outlined in Table 2, for the four different drive cycles. First of all, it can be seen that the average energy consumption varies for the drive cycles which is expected as they had different lengths and route profiles. Furthermore, it is evident that the examined parameters cause a significant variance in the required battery energy. As shown in Figure 22d $\sum S_i^G \approx \sum S_{T_i}^G$ holds for all four drive cycles which indicates a linear parameter dependency on the output E_b . This coincides with the qualitative Morris screening as already discussed in Section 6.1. Furthermore, it indicates that $S_i^G \approx S_{T_i}^G$, which means that the total and first-order effects are nearly equal. The first-order indices, as outlined in Figure 22b, show that only a few parameters are dominating the output variance. These are the rolling resistance coefficient c_r , the auxiliary losses P_{pto} , the vehicle mass m_v and the battery temperature ϑ_b . Another important finding is that the parameter belonging to the controller—and thus, can be influenced during the operation of the vehicle—only contributes a maximum of 5% to the overall variance. In other words, it can be confirmed that operating or pre-conditioning the battery in a suitable temperature range and reducing the mass of the vehicle has much stronger effect on the energy consumption than tuning

the parameters in an advanced control concept. However, the controller tuning parameter c_c can be used to affect the energy consumption most from the point of view of the control strategy. It is also important to mention that the sensitivities of the driving cycles do not differ greatly and that the vehicle behaves relatively similarly. One exception is the sensitivity of the battery temperature ϑ_b in drive cycle 3. This can be explained by the fact that less total energy or average power is converted in this drive cycle. Therefore, the ohmic battery losses and their dependence on the energy consumption do not have such a strong effect than for the other drive cycles.

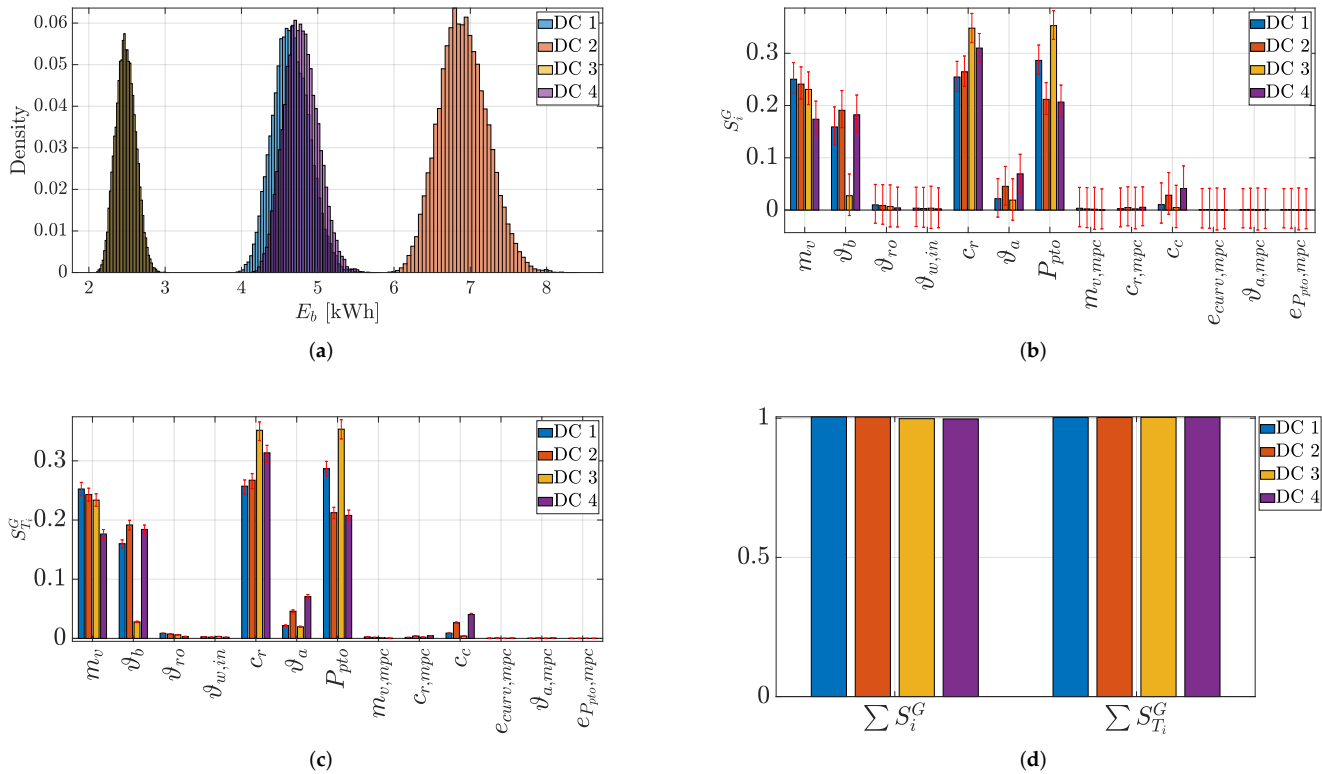


Figure 22. Generalized Sobol Indices and histograms for consumed battery energy E_b (a) Histograms, (b) First-order effects with 95% confidence interval, (c) Total effects with 95% confidence interval, (d) Sum of effects.

The next analyzed output of interest is P_l , which combines all losses occurring in the powertrain during operation. As can be seen from Figure 23a, the investigated parameters have a significant influence on the variance of P_l . The fact that $\sum S_i^G \neq \sum S_{T_i}^G$ holds for all drive cycles, as depicted in Figure 23d, underpins the results of the Morris screening in Section 6.1 that nonlinear or higher-order effects exist. From Figure 23d it can be inferred that approximately 80% of the variance are caused by first-order and the rest by nonlinear or interaction effects.

The first-order effects of the power losses are shown in Figure 23b. Here, the vehicle mass m_v and the battery temperature ϑ_b contribute significantly to the variance. However, beside the parameters related to the vehicle itself, it can be seen that the power losses are also influenced by the distribution of the estimated vehicle mass $m_{v,mpc}$. This parameter is considered as a measured or estimated controller input variable. In this case, a reduction in the variance of $m_{v,mpc}$ could reduce the variance in the power losses significantly. In other words, if $m_{v,mpc}$ is better estimated or measured, the variance in the power losses is also reduced. The choice of c_c also influences the power losses but the effect of this controller tuning parameter is rather small, compared to the parameters mentioned before.

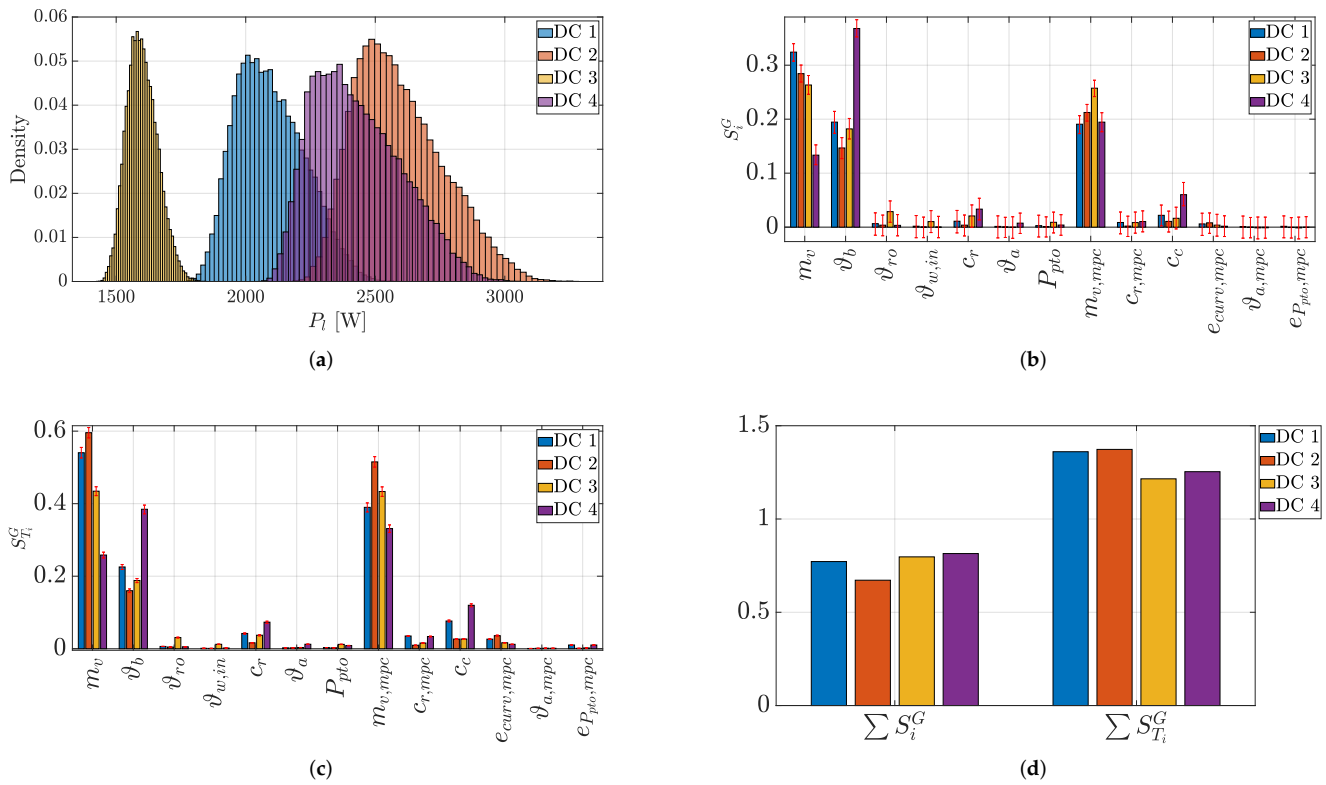


Figure 23. Generalized Sobol Indices and histograms for the total drive power losses P_l (a) Histograms, (b) First order effects with 95% confidence interval, (c) Total order effects with 95% confidence interval, (d) Sum of effects.

Another interesting output to look at is the total driving time t_d . This has a direct impact on the acceptance of a driver assistance system, as drivers are normally not willing to accept large increases in travel time. It can be seen that the investigated input parameters also caused a distribution of the driving time for the longitudinal control system as outlined in Figure 24a. The driving time behaves nearly linearly, as $\sum S_i^G \approx S_{T_i}^G$ holds, as outlined in Figure 24d. The nonlinear effects are negligibly small.

As the first-order effects of Figure 24b demonstrate, c_c has the biggest influence on the driving time in drive cycles 2 and 4 which are the most energy-consuming drive cycles. However, as outlined above, the controller parameter c_c has only a small effect on the energy consumption. Consequently, the travel time is mainly affected by c_c without consuming significantly more or less energy. Meanwhile, aside from c_c , the controller parameters $m_{v,mpc}$ and $c_{r,mpc}$ also have a significant influence on the driving time. Furthermore, the two vehicle parameters m_v and c_r clearly contribute to the distribution of t_d .

To summarize the above outlined results, it can be stated that only a few of the investigated parameters have a notable impact on the analyzed output. Nevertheless, this influence is significant and clearly visible in the variances of the output and could not be neglected. Overall, that the most important parameters belonging to the vehicle or its components are the vehicle mass m_v , the rolling resistance coefficient c_r and the battery temperature ϑ_b . From this, it is obvious that reducing the rolling resistance coefficient and also the mass of the vehicle will have a significant impact on the energy required by the vehicle. It is also shown that the battery temperature ϑ_b also plays an important role, regarding the energy efficiency of the powertrain. Influencing the battery temperature during operation is not directly possible, as the thermal mass of the battery is so big that the battery losses would cause a major temperature rise to heat up the battery. However it can be seen, from our investigation, that a possible solution could be to pre-condition the battery before driving the vehicle, in order to reduce energy losses in the battery system.

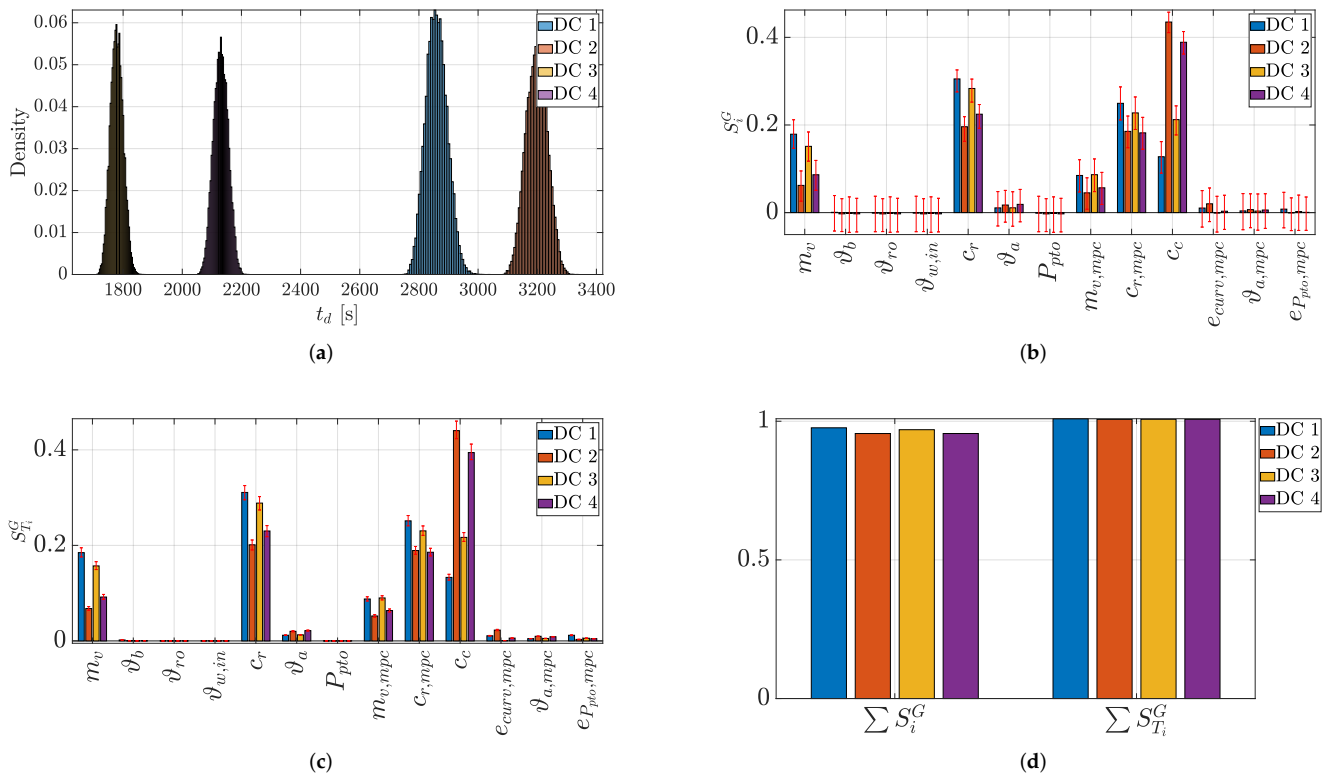


Figure 24. Generalized Sobol Indices and histograms for the total driving time t_d (a) Histograms, (b) First-order effects with 95% confidence interval, (c) Total effects with 95% confidence interval, (d) Sum of effects.

Furthermore, it is outlined that the controller parameters have less impact on the energy consumption than the vehicle parameters, but they also have energy-saving potential. It can be seen, especially from the driving time t_d , that the parameter c_c has a large influence. Additionally, on the other outputs, an influence could be considered, which leads to the assumption that c_c mainly affects the driving time, but it may possibly improve the energy consumption. It is also found that the measured or estimated mass of the vehicle $m_{v,mpc}$ and the rolling resistance $c_{r,mpc}$ cause a substantial amount of the variance in the driving time t_d , as well as that in the power losses P_l . As a consequence, these parameters should be estimated as accurately as possible, in order to improve the energy efficiency of the controller.

It is important to mention that the sensitivity analysis was performed for the controller proposed in Section 4. Thus, it is possible that, if the controller concept is modified, e.g., by changing the cost function or the constraints, the sensitivity analysis results will be affected. Similarly, the vehicle design can affect the results. For instance, with a heavier vehicle, the change in mass due to the number of people carried does not strongly affect the total mass much, in percentage terms. However, optimization of the vehicle is beyond the scope of this work.

It can be summarized that the investigated outputs behave differently regarding their parameter sensitivities. It should also be mentioned that the ranking, according to their importance, depends highly on the investigation or development target. The main interesting variables in this study for energy-efficient longitudinal motion control are the battery energy E_b and the driving time t_d . In contrast, if component loss optimization is the main development goal, the overall power losses P_l or some component-specific losses (e.g., battery losses), should be the main variables of interest. Due to this difference in prioritization, depending on the development goal, the model outputs of interest should be considered separately and not evaluated together.

7. Conclusions

In this article, a novel approach for analyzing complex closed-loop economic model predictive longitudinal control systems is presented. It is outlined that a qualitative screening method is able to generate a reduced set of parameters for variance-based sensitivity analysis, thus reducing the computational burden of the Monte-Carlo simulation. The use of Generalized Sobol Indices outlined the ability to deal with time-dependent processes. It is shown that only a small subset of the parameters are sensitive regarding the energy consumption, the power losses and the driving time. It can be concluded that the vehicle mass, the battery temperature and the rolling resistance of the vehicle have the biggest influence on the energy consumption of the modeled vehicle, whereas the influence of EMPC tuning factors is only small with the unpleasant side-effect of worsening the driving time. Furthermore, it is shown that good estimates in the EMPC of the vehicle mass and the rolling resistance could improve the controller performance by reducing the variance of the energy consumption and driving time. In general the used methods can be seen as powerful tools for quantifying the effects on an output of the system with respect to their cause. This will help researchers or developers to identify relevant parameters and focus on them to more effectively improve the overall system behavior.

Author Contributions: Conceptualization, M.B.; methodology, M.B.; software, M.B.; validation, M.B., M.S. and H.V.; formal analysis, M.B.; investigation, M.B.; resources, M.B.; data curation, M.B.; writing—original draft preparation, M.B.; writing—review and editing, M.B., M.S. and H.V.; visualization, M.B.; supervision, M.S. and H.V. All authors have read and agreed to the published version of the manuscript.

Funding: This research received no external funding.

Institutional Review Board Statement: Not applicable.

Informed Consent Statement: Not applicable.

Data Availability Statement: The data presented in this study are available on request from the corresponding author.

Conflicts of Interest: The authors declare no conflict of interest.

Abbreviations

The following abbreviations are used in this manuscript:

ANOVA	Analysis of variance
BEV	Battery electric vehicle
EMPC	Economic model predictive control
HDMR	High-dimensional model representation
IGBT	Insulated gate bipolar transistor
MPC	Model predictive control
NMPC	Nonlinear model predictive control
PMSM	Permanent magnet synchronous machine
PWM	Pulse width modulation
SoC	State of charge
VSI	Voltage source inverter

Appendix A

Appendix A.1. Longitudinal Motion Model

The longitudinal motion model considers the mechanical forces acting on a vehicle's center of gravity and a gearbox model transforming the mechanical energy of the electric drives to the wheels. The force equilibrium in the center of gravity of the vehicle is described by

$$F_L + F_R = F_a + F_r + F_s + F_{air}, \quad (A1)$$

where F_L and F_R are the forces acting on the left and right rear wheel which drive the vehicle. The driving resistance forces comprise the acceleration resistance force F_a , the rolling resistance force F_r , the slope resistance force F_s and the air resistance force F_{air} . The acceleration resistance force is caused by Newton’s second law. It is expressed by

$$F_a = m_{eq} \cdot a_{ego}, \tag{A2}$$

where m_{eq} denotes the equivalent mass, including the inertia of the rotating parts of the powertrain which belong to their kinetic energy. Furthermore, a_{ego} describes the acceleration of the vehicle. The rolling resistance can be described by

$$F_r = c_r \cdot m_v \cdot g \cdot \cos(\alpha) \quad \text{with} \quad v_{ego} > 0, \tag{A3}$$

where c_r denotes the rolling resistance coefficient and α is the road slope angle. In a similar manner, the resistance force caused by the road slope

$$F_s = m_v \cdot g \cdot \sin(\alpha) \tag{A4}$$

describes the additional force when driving up or downhill, with g being the gravitational constant. Additionally, the movement of the vehicle through the surrounding air causes the aerodynamic resistance force

$$F_{air} = \frac{1}{2} c_w \cdot A_v \cdot \rho_{air} \cdot v_{ego}^2 \tag{A5}$$

to act on the vehicle. This includes the aerodynamic drag coefficient c_w , the frontal area of the vehicle A_v and the air density ρ_{air} .

The conversion from the longitudinal motion model and the associated forces to the rotational model of the powertrain is achieved by the law of levers. The transformation from the longitudinal driving forces F_L and F_R to the corresponding drive shaft torques M_L and M_R of the wheels is given by

$$M_L = F_L \cdot r_w \tag{A6}$$

and

$$M_R = F_R \cdot r_w \tag{A7}$$

with the wheel radius r_w . Assuming, that the same torque is applied on the left and the right wheel the needed driving force in (A1) can be described by

$$F_R + F_L = \frac{M_L + M_R}{r_w} = 2M_D \quad \text{with} \quad M_W = M_L = M_R. \tag{A8}$$

The gearbox is modeled with a constant gear ratio i_g , using a working point dependent efficiency map $\eta_g(\omega_m, M_{em})$. This leads to

$$M_D = M_{em} \cdot i_g \cdot \eta_g(\omega_m, M_{em}), \tag{A9}$$

describing the transition from the mechanical torque of the electrical drives M_{em} to the torques M_D applied to the wheels. The parameters for the longitudinal motion model are provided in Table A1.

Table A1. Longitudinal motion model parameters.

Parameter	Description	Value
c_w	Air drag coefficient	0.262
A_v	Frontal area	2.036 m ²
m_v	Vehicle mass	550 kg
m_{eq}	Equivalent vehicle mass (including rotational inertia)	569 kg
r_w	Wheel radius	0.283 m
i_g	Gear ratio	5.85

References

1. Jayakumar, A.; Chalmers, A.; Lie, T.T. Review of prospects for adoption of fuel cell electric vehicles in New Zealand. *IET Electr. Syst. Transp.* **2017**, *7*, 259–266. [[CrossRef](#)]
2. Vaezipour, A.; Rakotonirainy, A.; Haworth, N. Reviewing In-vehicle Systems to Improve Fuel Efficiency and Road Safety. *Procedia Manuf.* **2015**, *3*, 3192–3199. [[CrossRef](#)]
3. Barkenbus, J.N. Eco-driving: An overlooked climate change initiative. *Energy Policy* **2010**, *38*, 762–769. [[CrossRef](#)]
4. Schwickart, T.; Voos, H.; Hadji-Minaglou, J.R.; Darouach, M.; Rosich, A. Design and simulation of a real-time implementable energy-efficient model-predictive cruise controller for electric vehicles. *J. Frankl. Inst.* **2015**, *352*, 603–625. [[CrossRef](#)]
5. Schwickart, T.; Voos, H.; Hadji-Minaglou, J.R.; Darouach, M. A Fast Model-Predictive Speed Controller for Minimised Charge Consumption of Electric Vehicles. *Asian J. Control* **2016**, *18*, 133–149. [[CrossRef](#)]
6. Naus, G.; Ploeg, J.; van de Molengraft, M.; Heemels, W.; Steinbuch, M. Design and implementation of parameterized adaptive cruise control: An explicit model predictive control approach. *Control Eng. Pract.* **2010**, *18*, 882–892. [[CrossRef](#)]
7. Jia, Y.; Jibrin, R.; Itoh, Y.; Görges, D. Energy-Optimal Adaptive Cruise Control for Electric Vehicles in Both Time and Space Domain based on Model Predictive Control. *IFAC-PapersOnLine* **2019**, *52*, 13–20. [[CrossRef](#)]
8. Kamal, M.A.S.; Mukai, M.; Murata, J.; Kawabe, T. Model Predictive Control of Vehicles on Urban Roads for Improved Fuel Economy. *IEEE Trans. Control Syst. Technol.* **2013**, *21*, 831–841. [[CrossRef](#)]
9. Caldas, K.A.Q.; Grassi, V. Eco-cruise NMPC Control for Autonomous Vehicles. In Proceedings of the 19th International Conference on Advanced Robotics (ICAR), Belo Horizonte, Brazil, 2–6 December 2019; IEEE: New York, NY, USA, 2019; pp. 356–361. [[CrossRef](#)]
10. Chen, Y.; Li, X.; Wiet, C.; Wang, J. Energy Management and Driving Strategy for In-Wheel Motor Electric Ground Vehicles with Terrain Profile Preview. *IEEE Trans. Ind. Inform.* **2014**, *10*, 1938–1947. [[CrossRef](#)]
11. Weißmann, A.; Görges, D.; Lin, X. Energy-Optimal Adaptive Cruise Control based on Model Predictive Control. *IFAC-PapersOnLine* **2017**, *50*, 12563–12568. [[CrossRef](#)]
12. Sajadi-Alamdari, S.A.; Voos, H.; Darouach, M. Nonlinear model predictive extended eco-cruise control for battery electric vehicles. In Proceedings of the 24th Mediterranean Conference on Control and Automation (MED), Athens, Greece, 21–24 June 2016; IEEE: New York, NY, USA, 2016; pp. 467–472. [[CrossRef](#)]
13. Vajedi, M.; Azad, N.L. Ecological Adaptive Cruise Controller for Plug-In Hybrid Electric Vehicles Using Nonlinear Model Predictive Control. *IEEE Trans. Intell. Transp. Syst.* **2016**, *17*, 113–122. [[CrossRef](#)]
14. Frezza, G.; Evangelou, S.A. Ecological Adaptive Cruise Controller for a Parallel Hybrid Electric Vehicle. In Proceedings of the European Control Conference (ECC), St. Petersburg, Russia, 12–15 May 2020; IEEE: New York, NY, USA, 2020; pp. 491–498. [[CrossRef](#)]
15. Sajadi-Alamdari, S.A.; Voos, H.; Darouach, M. Risk-averse Stochastic Nonlinear Model Predictive Control for Real-time Safety-critical Systems. *IFAC-PapersOnLine* **2017**, *50*, 5991–5997. [[CrossRef](#)]
16. Sajadi-Alamdari, S.A.; Voos, H.; Darouach, M. Fast stochastic non-linear model predictive control for electric vehicle advanced driver assistance systems. In Proceedings of the IEEE International Conference on Vehicular Electronics and Safety (ICVES), Vienna, Austria, 27–28 June 2017; IEEE: New York, NY, USA, 2017; pp. 91–96. [[CrossRef](#)]
17. Sajadi-Alamdari, S.A.; Voos, H.; Darouach, M. Nonlinear Model Predictive Control for Ecological Driver Assistance Systems in Electric Vehicles. *Robot. Auton. Syst.* **2019**, *112*, 291–303. [[CrossRef](#)]
18. Moser, D.; Waschl, H.; Kirchsteiger, H.; Schmied, R.; del Re, L. Cooperative adaptive cruise control applying stochastic linear model predictive control strategies. In Proceedings of the European Control Conference (ECC), Linz, Austria, 15–17 July 2015; IEEE: New York, NY, USA, 2015; pp. 3383–3388. [[CrossRef](#)]
19. Moser, D.; Schmied, R.; Waschl, H.; del Re, L. Flexible Spacing Adaptive Cruise Control Using Stochastic Model Predictive Control. *IEEE Trans. Control Syst. Technol.* **2018**, *26*, 114–127. [[CrossRef](#)]
20. Morris, M.D. Factorial Sampling Plans for Preliminary Computational Experiments. *Technometrics* **1991**, *33*, 161–174. [[CrossRef](#)]
21. Sobol, I.M. Sensitivity Analysis for Nonlinear Mathematical Models. *Math. Model. Comput. Exp.* **1993**, *1*, 407–414.
22. Vepsäläinen, J.; Ritari, A.; Lajunen, A.; Kivekäs, K.; Tammi, K. Energy Uncertainty Analysis of Electric Buses. *Energies* **2018**, *11*, 3267. [[CrossRef](#)]
23. Vepsäläinen, J.; Otto, K.; Lajunen, A.; Tammi, K. Computationally efficient model for energy demand prediction of electric city bus in varying operating conditions. *Energy* **2019**, *169*, 433–443. [[CrossRef](#)]
24. Asamer, J.; Graser, A.; Heilmann, B.; Ruthmair, M. Sensitivity analysis for energy demand estimation of electric vehicles. *Transp. Res. Part Transp. Environ.* **2016**, *46*, 182–199. [[CrossRef](#)]
25. Zhao, S.; Howey, D.A. Global Sensitivity Analysis of Battery Equivalent Circuit Model Parameters. In Proceedings of the IEEE Vehicle Power and Propulsion Conference (VPPC), Hangzhou, China, 17–20 October 2016; IEEE: New York, NY, USA, 2016; pp. 1–4. [[CrossRef](#)]
26. Grandjean, T.R.B.; Li, L.; Odio, M.X.; Widanage, W.D. Global Sensitivity Analysis of the Single Particle Lithium-Ion Battery Model with Electrolyte. In Proceedings of the IEEE Vehicle Power and Propulsion Conference (VPPC), Hanoi, Vietnam, 14–17 October 2019; IEEE: New York, NY, USA, 2019; pp. 1–7. [[CrossRef](#)]
27. Braband, M.; Adams, M.; Wilhelmi, A.; Scherer, M. Global Sensitivity Analysis on the Torque Accuracy of the Powertrain in Electric Vehicles. *IFAC-PapersOnLine* **2020**, *53*, 14067–14072. [[CrossRef](#)]

28. Asef, P.; Laphorn, A. Overview of Sensitivity Analysis Methods Capabilities for Traction AC Machines in Electrified Vehicles. *IEEE Access* **2021**, *9*, 23454–23471. [[CrossRef](#)]
29. Saltelli, A.; Aleksankina, K.; Becker, W.; Fennell, P.; Ferretti, F.; Holst, N.; Li, S.; Wu, Q. Why so many published sensitivity analyses are false: A systematic review of sensitivity analysis practices. *Environ. Model. Softw.* **2019**, *114*, 29–39. [[CrossRef](#)]
30. Alexanderian, A.; Gremaud, P.A.; Smith, R.C. Variance-based sensitivity analysis for time-dependent processes. *Reliab. Eng. Syst. Saf.* **2020**, *196*, 106722. [[CrossRef](#)]
31. Campolongo, F.; Saltelli, A. Sensitivity analysis of an environmental model: An application of different analysis methods. *Reliab. Eng. Syst. Saf.* **1997**, *57*, 49–69. [[CrossRef](#)]
32. Campolongo, F.; Tarantola, S.; Saltelli, A. Tackling quantitatively large dimensionality problems. *Comput. Phys. Commun.* **1999**, *117*, 75–85. [[CrossRef](#)]
33. Campolongo, F.; Cariboni, J.; Saltelli, A. An effective screening design for sensitivity analysis of large models. *Environ. Model. Softw.* **2007**, *22*, 1509–1518. [[CrossRef](#)]
34. Saltelli, A.; Annoni, P.; Azzini, I.; Campolongo, F.; Ratto, M.; Tarantola, S. Variance based sensitivity analysis of model output. Design and estimator for the total sensitivity index. *Comput. Phys. Commun.* **2010**, *181*, 259–270. [[CrossRef](#)]
35. Homma, T.; Saltelli, A. Importance measures in global sensitivity analysis of nonlinear models. *Reliab. Eng. Syst. Saf.* **1996**, *52*, 1–17. [[CrossRef](#)]
36. Gamboa, F.; Janon, A.; Klein, T.; Lagnoux, A. Sensitivity analysis for multidimensional and functional outputs. *Electron. J. Stat.* **2014**, *8*, 575–603. [[CrossRef](#)]
37. Doyle, M.; Fuller, T.F.; Newman, J. Modeling of Galvanostatic Charge and Discharge of the Lithium/Polymer/Insertion Cell. *J. Electrochem. Soc.* **1993**, *140*, 1526–1533. [[CrossRef](#)]
38. Fuller, T.F.; Doyle, M.; Newman, J. Simulation and Optimization of the Dual Lithium Ion Insertion Cell. *J. Electrochem. Soc.* **1994**, *141*, 1–10. [[CrossRef](#)]
39. Krewer, U.; Röder, F.; Harinath, E.; Braatz, R.D.; Bedürftig, B.; Findeisen, R. Review—Dynamic Models of Li-Ion Batteries for Diagnosis and Operation: A Review and Perspective. *J. Electrochem. Soc.* **2018**, *165*, A3656–A3673. [[CrossRef](#)]
40. Zhao, R.; Kollmeyer, P.J.; Lorenz, R.D.; Jahns, T.M. A Compact Methodology Via a Recurrent Neural Network for Accurate Equivalent Circuit Type Modeling of Lithium-Ion Batteries. *IEEE Trans. Ind. Appl.* **2019**, *55*, 1922–1931. [[CrossRef](#)]
41. Chiasserini, C.F.; Rao, R.R. Energy efficient battery management. *IEEE J. Sel. Areas Commun.* **2001**, *19*, 1235–1245. [[CrossRef](#)]
42. Hageman, S.C. Simple PSpice models let you simulate common battery types. *Electron. Des. News* **1993**, *38*, 117–129.
43. Hentunen, A.; Lehmuspelto, T.; Suomela, J. Time-Domain Parameter Extraction Method for Thévenin-Equivalent Circuit Battery Models. *IEEE Trans. Energy Convers.* **2014**, *29*, 558–566. [[CrossRef](#)]
44. Hamm, P. Thermische Charakterisierung und Evaluierung einer LiFePO₄-Batteriezele. Master's Thesis, University of Applied Sciences, Trier, Germany, 2021.
45. Lehnertz, M. Entwicklung eines Schätzverfahrens zur Bestimmung der Inneren Zelltemperatur von LiFePO₄ Batteriezele. Master's Thesis, University of Applied Sciences, Trier, Germany, 2021.
46. Kolar, J.W.; Ertl, H.; Zach, F.C. Influence of the modulation method on the conduction and switching losses of a PWM converter system. *IEEE Trans. Ind. Appl.* **1991**, *27*, 502–512. [[CrossRef](#)]
47. Schröder, D. *Elektrische Antriebe—Regelung von Antriebssystemen*, 4th ed.; Springer: Berlin/Heidelberg, Germany, 2015. [[CrossRef](#)]
48. Drogenik, U.; Kolar, J.W. A general scheme for calculating switching-and conduction-losses of power semiconductors in numerical circuit simulations of power electronic systems. *Proc. IPEC* **2005**, *5*, 4–8.
49. Bierhoff, M.H.; Fuchs, F.W. Semiconductor losses in voltage source and current source IGBT converters based on analytical derivation. In Proceedings of the IEEE 35th Annual Power Electronics Specialists Conference, Aachen, Germany, 20–25 June 2004; IEEE: New York, NY, USA, 2004; pp. 2836–2842. [[CrossRef](#)]
50. Infineon Technologies AG. *HybridPACK Drive Module FS820R08A6P2: Final Data Sheet, V3.3*; Infineon Technologies: Neubiberg, Germany, 2019.
51. Windisch, T.; Hofmann, W. Energieeffiziente Regelung von Fahrzeugantrieben mit permanenterregten Synchron- und Asynchronmotoren unter Berücksichtigung von Umrichter, Eisenverlusten und Sättigung. In *Elektrische Antriebstechnologie Für Hybrid-Und Elektrofahrzeuge*; Schäfer, H., Ed.; Springer: Berlin/Heidelberg, Germany, 2019; pp. 218–237.
52. Baehr, H.D.; Stephan, K. *Wärme-Und Stoffübertragung*, 8th ed.; Springer: Berlin/Heidelberg, Germany, 2013. doi: [[CrossRef](#)]
53. Schröder, D. *Elektrische Antriebe—Grundlagen*, 5th ed.; Springer: Berlin/Heidelberg, Germany, 2013. [[CrossRef](#)]
54. Kellner, S.L.; Seilmeier, M.; Piepenbreier, B. Impact of iron losses on parameter identification of permanent magnet synchronous machines. In Proceedings of the 1st International Electric Drives Production Conference, Nuremberg, Germany, 28–29 September 2011; IEEE: New York, NY, USA, 2011; pp. 11–16. [[CrossRef](#)]
55. Kellner, S.L. Parameteridentifikation bei Permanenterregten Synchronmaschinen. Ph.D. Thesis, University of Erlangen-Nuremberg, Erlangen, Germany, 2012.
56. HERE Technologies. HERE Plattform. Available online: <https://www.here.com/platform> (accessed on 22 January 2022)
57. Kohut, N.J.; Karl Hedrick, P.J.; Borrelli, P.F. Integrating Traffic Data and Model Predictive Control to Improve Fuel Economy. *IFAC Proc. Vol.* **2009**, *42*, 155–160. [[CrossRef](#)]
58. Faulwasser, T.; Grüne, L.; Müller, M.A. Economic Nonlinear Model Predictive Control. *Found. Trends Syst. Control* **2018**, *5*, 1–98. [[CrossRef](#)]

-
59. Verschueren, R.; Frison, G.; Kouzoupis, D.; Frey, J.; van Duijkeren, N.; Zanelli, A.; Novoselnik, B.; Albin, T.; Quirynen, R.; Diehl, M. acados—A modular open-source framework for fast embedded optimal control. *Math. Program. Comput.* **2022**, *14*, 147–183. [[CrossRef](#)]
 60. Schwickart, T.K. Energy-Efficient Driver Assistance System for Electric Vehicles Using Model-Predictive Control. Ph.D. Thesis, University of Luxembourg, Luxembourg, 2015.